

# A coupled global–local shell model with continuous interlaminar shear stresses

F. Gruttmann<sup>1</sup> · W. Wagner<sup>2</sup> · G. Knust<sup>1</sup>

Received: 24 September 2015 / Accepted: 12 November 2015 / Published online: 11 December 2015  
© Springer-Verlag Berlin Heidelberg 2015

**Abstract** In this paper layered composite shells subjected to static loading are considered. The theory is based on a multi-field functional, where the associated Euler–Lagrange equations include besides the global shell equations formulated in stress resultants, the local in-plane equilibrium in terms of stresses and a constraint which enforces the correct shape of warping through the thickness. Within a four-node element the warping displacements are interpolated with layerwise cubic functions in thickness direction and constant shape throughout the element reference surface. Elimination of stress, warping and Lagrange parameters on element level leads to a mixed hybrid shell element with 5 or 6 nodal degrees of freedom. The implementation in a finite element program is simple. The computed interlaminar shear stresses are automatically continuous at the layer boundaries. Also the stress boundary conditions at the outer surfaces are fulfilled and the integrals of the shear stresses coincide exactly with the independently interpolated shear forces without introduction of further constraints. The essential feature of the element formulation is the fact that it leads to usual shell degrees of freedom, which allows application of standard boundary or symmetry conditions and computation of shell structures with intersections.

**Keywords** Layered composite shells · Mixed variational formulation · Continuous interlaminar shear stresses · Standard shell degrees of freedom

✉ W. Wagner  
w.wagner@kit.edu

<sup>1</sup> Fachgebiet Festkörpermechanik, Technische Universität Darmstadt, Franziska-Braun-Str. 7, 64287 Darmstadt, Germany

<sup>2</sup> Institut für Baustatik, Karlsruher Institut für Technologie, Kaiserstr. 12, 76131 Karlsruhe, Germany

## 1 Introduction

A survey on models to compute the complete three-dimensional stress state in laminates is given e.g. in [1–5]. In the following only a few representative papers out of a large number are discussed.

Shell theories are able to describe the overall deformation behaviour of thin laminated structures. Nowadays mostly the first-order shear deformation theory is the accepted basis to develop elements. This theory considers also shear deformations, which is essential in the context of composite structures. It needs only  $C^0$ - instead of  $C^1$ -continuity, being of great interest from a numerical point of view. Often this approach gives satisfactory results for a wide class of structural problems, even for moderately thick laminates and should be the best compromise between prediction ability and computational costs. For thin up to moderately thick structures one obtains sufficiently accurate in-plane stresses, however the interlaminar stresses are either zero or only averaged values are obtained.

If one is interested in more local problems—e.g. the question of construction of connections or the description of the interlaminar stresses—the use of standard two-dimensional models is not appropriate. Highly complicated inter- and intralaminar failure modes (e.g. delamination and ply failure) may occur in laminated structures which could considerably influence the overall structural behaviour. In order to obtain the complicated three-dimensional stress state in layered structures various approaches have been developed. Especially the interlaminar stresses are of interest for the evaluation of failure criteria.

Several authors exploit the equilibrium equations within a post-processing technique, e.g. [6, 7]. The computed interlaminar stresses are not embedded in the variational formulation. These techniques have also been used in conjunc-

tion with commercial codes. Besides a predictor corrector approach [8], the equilibrium equations have been successfully exploited, e.g. [9]. In general, this requires higher-order shape functions to allow for second order derivatives of the in-plane stresses. Thus typically elements with bi-quadratic or bi-cubic shape functions are used, e.g. [10]. In [11] a proper generalized decomposition and layer-wise approach for the modelling of composite plate structures is proposed.

The authors in [12–14] present linear plate elements based on mixed-enhanced approaches. On basis of the first-order shear deformation theory resultant shear stresses and enhanced incompatible modes are used as primary variables.

In [15] and [16] refined theories with seven unknown kinematic quantities have been presented. The standard displacement field is enhanced by layer-wise linear (zig-zag) functions through the thickness. For an overview on zig-zag theories for multilayered plates and shells see e.g. [17].

Higher order plate and shell formulations and layerwise theories have been developed to obtain an accurate shape of the interlaminar stresses, e.g. [18–25]. For example, Ref. [18] accounts for a parabolic distribution of the transverse shear strains through the thickness of the plate. For geometrical nonlinear formulations we refer to e.g. [26, 27].

The use of brick elements or so-called solid shell elements, e.g. [28–30] represents a computationally expensive approach. For a sufficient accurate evaluation of the interlaminar stresses each layer must be discretised with several elements ( $\approx 5$ – $10$ ) in thickness direction. The price for this type of modelling is a large number of unknowns leading to unacceptable computing times. Especially for non-linear practical problems with a multiplicity of load steps and several iterations in each load step this is not a feasible approach.

Based on above discussion we propose a shell formulation which is characterized by the following features and new developments.

- (i) The underlying shell theory is based on the Reissner–Mindlin kinematics with inextensible director field. This leads in the basic version to averaged transverse shear strains when exploiting the linearised Green–Lagrangian strain tensor. The extension to geometrical nonlinearity for the *global part* of the formulation is a straight forward task, see e.g. [31, 32]. For the sake of convenience, here we restrict to the linear representation.
- (ii) We propose a multi-field functional, where the associated Euler–Lagrange equations include besides the usual shell equations in terms of stress resultants the local inplane equilibrium in terms of stresses and a constraint which enforces the correct shape of the warping function through the thickness.
- (iii) The displacements of the Reissner–Mindlin kinematics are enriched by a fluctuation field, which describes

warping. Within four-node elements the warping displacements are formed with layerwise cubic functions through the thickness and constant distribution throughout the element reference surface.

- (iv) Elimination of stress, warping and Lagrange parameters on element level leads to a mixed hybrid shell element. The condensation is computationally effective since the relevant matrices are sparse. The resulting element stiffness matrix for quadrilaterals exhibits the usual 5 or 6 nodal degrees of freedom. This is an essential property since standard geometrical boundary conditions can be applied and the element is applicable also to shell intersection problems. Due to the simple structure of the formulation the implementation in a finite element program can easily be achieved.
- (v) Without introduction of further constraints continuity of the interlaminar shear stresses is *automatically* obtained in an exact way. This holds also for the zero stress conditions at the outer surfaces and for the integrals of the shear stresses which coincide identically with the independently interpolated shear forces.
- (vi) The computed interlaminar shear stresses show good agreement with the results of costly 3D-computations. Likewise comparisons with the post processing procedure [7] are performed. In contrast to that approach, here the interlaminar shear stresses are embedded in the variational formulation.

The paper is organized as follows. In Sect. 2 we propose a functional and derive the first variation as well as the associated Euler–Lagrange equations. The shape of the warping displacements, the integrals in thickness direction of the constitutive law assuming orthotropic material behaviour and the constraint are specified in Sect. 3. Furthermore the approximations of the independent fields and the derivation of a mixed-hybrid element stiffness matrix is shown. The membrane and bending patch test, a plate with 5 different layer sequences and a stiffened cylindrical shell are investigated in Sect. 4.

## 2 Functional and Euler–Lagrange equations

Let  $\mathcal{B}$  be the three-dimensional Euclidean space occupied by a shell with thickness  $h$ . With  $\xi^i$  we denote a convected coordinate system of the body, where for the thickness coordinate holds  $h^- \leq \xi^3 \leq h^+$ . For the reference surface  $\Omega$  of the shell holds  $\xi^3 = 0$  and the coordinate on the boundary  $\Gamma$  is denoted by  $s$ . In the following the summation convention is used for repeated indices, where Latin indices range from 1 to 3 and Greek indices range from 1 to 2. Commas denote partial differentiation with respect to the coordinates  $\xi^\alpha$ .

The position vector of the reference surface is denoted by  $\mathbf{X}(\xi^1, \xi^2)$ . Furthermore, the vector field  $\bar{\mathbf{D}}(\xi^1, \xi^2)$  with  $|\bar{\mathbf{D}}(\xi^1, \xi^2)| = 1$  which is perpendicular to  $\Omega$  is introduced. The director field of the deformed configuration with position vector  $\mathbf{x}$  follows from  $\mathbf{d}(\xi^1, \xi^2) = \bar{\mathbf{D}} + \Delta\mathbf{d}$ . With  $\mathbf{d} \cdot \mathbf{x}_{,\alpha} \neq 0$  the kinematic assumption accounts for averaged transverse shear strains. Hence the displacements of the reference surface follow from  $\mathbf{u} = \mathbf{x} - \mathbf{X}$ . Based on the standard shell kinematics one can express the relation of the linearised Green–Lagrangian strains  $E_{ij}$  at a coordinate  $\xi^3$  to the shell strains by

$$\mathbf{E}_g = \mathbf{A}_1 \boldsymbol{\varepsilon}_g \quad \mathbf{E}_g = \begin{bmatrix} E_{11} \\ E_{22} \\ 2E_{12} \\ 2E_{13} \\ 2E_{23} \end{bmatrix}_g$$

$$\mathbf{A}_1 = \begin{bmatrix} 1 & 0 & 0 & \xi^3 & 0 & 0 & 0 & 0 \\ 0 & 1 & 0 & 0 & \xi^3 & 0 & 0 & 0 \\ 0 & 0 & 1 & 0 & 0 & \xi^3 & 0 & 0 \\ 0 & 0 & 0 & 0 & 0 & 0 & 1 & 0 \\ 0 & 0 & 0 & 0 & 0 & 0 & 0 & 1 \end{bmatrix}. \quad (1)$$

Here, the index  $g$  refers to geometrical strains and

$$\boldsymbol{\varepsilon}_g(\mathbf{v}) = [\varepsilon_{11}, \varepsilon_{22}, 2\varepsilon_{12}, \kappa_{11}, \kappa_{22}, 2\kappa_{12}, \gamma_1, \gamma_2]^T \quad (2)$$

with  $\mathbf{v} = [\mathbf{u}, \Delta\mathbf{d}]^T$ . The membrane strains, curvatures and transverse shear strains are given by

$$\varepsilon_{\alpha\beta} = \frac{1}{2}(\mathbf{u}_{,\alpha} \cdot \mathbf{X}_{,\beta} + \mathbf{u}_{,\beta} \cdot \mathbf{X}_{,\alpha})$$

$$\kappa_{\alpha\beta} = \frac{1}{2}(\mathbf{u}_{,\alpha} \cdot \bar{\mathbf{D}}_{,\beta} + \mathbf{u}_{,\beta} \cdot \bar{\mathbf{D}}_{,\alpha} + \mathbf{X}_{,\alpha} \cdot \Delta\mathbf{d}_{,\beta} + \mathbf{X}_{,\beta} \cdot \Delta\mathbf{d}_{,\alpha})$$

$$\gamma_\alpha = \mathbf{u}_{,\alpha} \cdot \bar{\mathbf{D}} + \mathbf{X}_{,\alpha} \cdot \Delta\mathbf{d}, \quad (3)$$

respectively.

We summarize the independent field quantities in the vector  $\boldsymbol{\theta} := [\mathbf{v}, \boldsymbol{\sigma}, \boldsymbol{\varepsilon}]^T$ . The vector of independent stress resultants reads

$$\boldsymbol{\sigma} = [n^{11}, n^{22}, n^{12}, m^{11}, m^{22}, m^{12}, q^1, q^2]^T \quad (4)$$

with membrane forces  $n^{\alpha\beta} = n^{\beta\alpha}$ , bending moments  $m^{\alpha\beta} = m^{\beta\alpha}$  and shear forces  $q^\alpha$ . The vector  $\boldsymbol{\varepsilon} = [\boldsymbol{\varepsilon}_1, \boldsymbol{\varepsilon}_2, \boldsymbol{\varepsilon}_3]^T$  consist of three parts. Note, that  $\boldsymbol{\varepsilon}_1$  contains physical shell strains,  $\boldsymbol{\varepsilon}_2$  discrete warping displacements and  $\boldsymbol{\varepsilon}_3$  Lagrange parameters. The three parts are formally summarized in the vector  $\boldsymbol{\varepsilon}$ . The components of the first part are organized in a sequence as in (2), whereas the components of the second and third part are specified in detail in the next section.

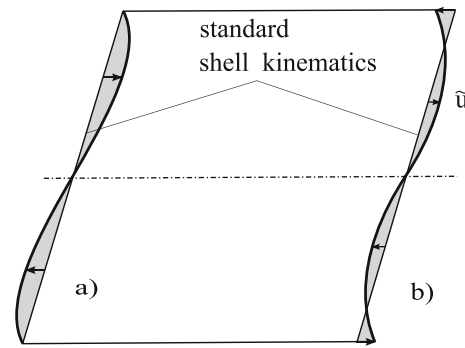


**Fig. 1** a Wrong shape and b qualitative correct shape of the warping function

We introduce the following functional depending on  $\boldsymbol{\theta} = [\mathbf{v}, \boldsymbol{\sigma}, \boldsymbol{\varepsilon}]^T$

$$\Pi(\boldsymbol{\theta}) = \int_{\Omega} [W(\boldsymbol{\varepsilon}_1, \boldsymbol{\varepsilon}_2) + \boldsymbol{\sigma}^T(\boldsymbol{\varepsilon}_g(\mathbf{v}) - \boldsymbol{\varepsilon}_1) + \boldsymbol{\varepsilon}_3^T \mathbf{g}(\boldsymbol{\varepsilon}_2)] dA + \Pi_{ext}(\mathbf{u}) \rightarrow \text{stat}. \quad (5)$$

Here, the area element of the reference surface is given by  $dA = j d\xi^1 d\xi^2$  and  $j = |\mathbf{X}_{,1} \times \mathbf{X}_{,2}|$ . The shell is loaded statically by surface loads  $\bar{\mathbf{p}}$  on  $\Omega$  and by boundary forces  $\bar{\mathbf{t}}$  on the boundary  $\Gamma_\sigma$ . Hence, the potential of the external loads reads

$$\Pi_{ext}(\mathbf{u}) = - \int_{\Omega} \mathbf{u}^T \bar{\mathbf{p}} dA - \int_{\Gamma_\sigma} \mathbf{u}^T \bar{\mathbf{t}} ds. \quad (6)$$

The strain energy density  $W$  is assumed to be a quadratic form in terms of  $\boldsymbol{\varepsilon}_\alpha$ , thus

$$W(\boldsymbol{\varepsilon}_1, \boldsymbol{\varepsilon}_2) = \frac{1}{2} \sum_{\alpha=1}^2 \sum_{\beta=1}^2 \boldsymbol{\varepsilon}_\alpha^T \mathbf{D}_{\alpha\beta} \boldsymbol{\varepsilon}_\beta. \quad (7)$$

The descriptive meaning of the constraint

$$\mathbf{g}(\boldsymbol{\varepsilon}_2) = \mathbf{D}_{32} \boldsymbol{\varepsilon}_2 = \mathbf{0} \quad (8)$$

is illustrated in Fig. 1. The warping function of Fig. 1a leads to additional bending moments and therefore is not correct. In Fig. 1b a qualitative correct shape is shown. Thus,  $\mathbf{g} = \mathbf{0}$  describes an orthogonality condition which enforces the correct shape of warping through the thickness, see Sect. 3.2. The constant matrices  $\mathbf{D}_{\alpha\beta}$  and  $\mathbf{D}_{32}$  are specified in the next section. The Lagrange term in (5) with constraint  $\mathbf{g} = \mathbf{0}$  represents an enhancement of the three-field functional introduced in Ref. [31].

With admissible variations  $\delta\boldsymbol{\theta} := [\delta\mathbf{v}, \delta\boldsymbol{\sigma}, \delta\boldsymbol{\varepsilon}]^T$  where  $\delta\mathbf{v} := [\delta\mathbf{u}, \delta\boldsymbol{\varphi}]^T$  the stationary condition for functional (5) reads

$$\begin{aligned} \delta\Pi(\boldsymbol{\theta}, \delta\boldsymbol{\theta}) &= \int_{\Omega} \left[ \left( \sum_{\alpha=1}^2 \delta\boldsymbol{\varepsilon}_{\alpha}^T \frac{\partial W}{\partial \boldsymbol{\varepsilon}_{\alpha}} \right) + \delta\boldsymbol{\sigma}^T (\boldsymbol{\varepsilon}_g - \boldsymbol{\varepsilon}_1) \right. \\ &\quad \left. + \delta\boldsymbol{\varepsilon}_g^T \boldsymbol{\sigma} - \delta\boldsymbol{\varepsilon}_1^T \boldsymbol{\sigma} + \delta\boldsymbol{\varepsilon}_3^T \mathbf{g} + \delta\boldsymbol{\varepsilon}_2^T \left( \frac{\partial \mathbf{g}}{\partial \boldsymbol{\varepsilon}_2} \right)^T \boldsymbol{\varepsilon}_3 \right] dA \\ &\quad + \delta\Pi_{ext} = 0 \end{aligned} \tag{9}$$

with  $\delta\Pi_{ext} = - \int_{\Omega} \delta\mathbf{u}^T \bar{\mathbf{p}} dA - \int_{\Gamma_{\sigma}} \delta\mathbf{u}^T \bar{\mathbf{t}} ds$ .

The virtual shell strains  $\delta\boldsymbol{\varepsilon}_g = [\delta\varepsilon_{11}, \delta\varepsilon_{22}, 2\delta\varepsilon_{12}, \delta\kappa_{11}, \delta\kappa_{22}, 2\delta\kappa_{12}, \delta\gamma_1, \delta\gamma_2]^T$  are given with

$$\begin{aligned} \delta\varepsilon_{\alpha\beta} &= \frac{1}{2}(\delta\mathbf{u}_{,\alpha} \cdot \mathbf{X}_{,\beta} + \delta\mathbf{u}_{,\beta} \cdot \mathbf{X}_{,\alpha}) \\ \delta\kappa_{\alpha\beta} &= \frac{1}{2}(\delta\mathbf{u}_{,\alpha} \cdot \bar{\mathbf{D}}_{,\beta} + \delta\mathbf{u}_{,\beta} \cdot \bar{\mathbf{D}}_{,\alpha} + \mathbf{X}_{,\alpha} \cdot \delta\mathbf{d}_{,\beta} + \mathbf{X}_{,\beta} \cdot \delta\mathbf{d}_{,\alpha}) \\ \delta\gamma_{\alpha} &= \delta\mathbf{u}_{,\alpha} \cdot \bar{\mathbf{D}} + \mathbf{X}_{,\alpha} \cdot \delta\mathbf{d} \end{aligned} \tag{10}$$

where  $\delta\mathbf{d} = \delta\boldsymbol{\varphi} \times \bar{\mathbf{D}}$  and  $\delta\mathbf{d}_{,\alpha} = \delta\boldsymbol{\varphi}_{,\alpha} \times \bar{\mathbf{D}}$ . Inserting (8) and

$$\frac{\partial W}{\partial \boldsymbol{\varepsilon}_{\alpha}} = \sum_{\beta=1}^2 \mathbf{D}_{\alpha\beta} \boldsymbol{\varepsilon}_{\beta} \quad \left( \frac{\partial \mathbf{g}}{\partial \boldsymbol{\varepsilon}_2} \right)^T = \mathbf{D}_{32}^T := \mathbf{D}_{23} \tag{11}$$

in Eq. (9) yields

$$\begin{aligned} \delta\Pi(\boldsymbol{\theta}, \delta\boldsymbol{\theta}) &= \int_{\Omega} \left[ \left( \sum_{\alpha=1}^2 \sum_{\beta=1}^2 \delta\boldsymbol{\varepsilon}_{\alpha}^T \mathbf{D}_{\alpha\beta} \boldsymbol{\varepsilon}_{\beta} \right) + \delta\boldsymbol{\sigma}^T (\boldsymbol{\varepsilon}_g - \boldsymbol{\varepsilon}_1) + \delta\boldsymbol{\varepsilon}_g^T \boldsymbol{\sigma} \right. \\ &\quad \left. - \delta\boldsymbol{\varepsilon}_1^T \boldsymbol{\sigma} + \delta\boldsymbol{\varepsilon}_3^T \mathbf{D}_{32} \boldsymbol{\varepsilon}_2 + \delta\boldsymbol{\varepsilon}_2^T \mathbf{D}_{23} \boldsymbol{\varepsilon}_3 \right] dA + \delta\Pi_{ext} \\ &= \int_{\Omega} \begin{bmatrix} \delta\boldsymbol{\varepsilon}_g \\ \delta\boldsymbol{\sigma} \\ \delta\boldsymbol{\varepsilon}_1 \\ \delta\boldsymbol{\varepsilon}_2 \\ \delta\boldsymbol{\varepsilon}_3 \end{bmatrix}^T \left\{ \begin{bmatrix} \mathbf{0} & \mathbf{1} & \mathbf{0} & \mathbf{0} & \mathbf{0} \\ \mathbf{1} & \mathbf{0} & -\mathbf{1} & \mathbf{0} & \mathbf{0} \\ \mathbf{0} & -\mathbf{1} & \mathbf{D}_{11} & \mathbf{D}_{12} & \mathbf{0} \\ \mathbf{0} & \mathbf{0} & \mathbf{D}_{21} & \mathbf{D}_{22} & \mathbf{D}_{23} \\ \mathbf{0} & \mathbf{0} & \mathbf{0} & \mathbf{D}_{32} & \mathbf{0} \end{bmatrix} \begin{bmatrix} \boldsymbol{\varepsilon}_g \\ \boldsymbol{\sigma} \\ \boldsymbol{\varepsilon}_1 \\ \boldsymbol{\varepsilon}_2 \\ \boldsymbol{\varepsilon}_3 \end{bmatrix} \right\} \\ &\quad \times dA + \delta\Pi_{ext} = 0. \end{aligned} \tag{12}$$

Introducing

$$\mathbf{D} := \begin{bmatrix} \mathbf{D}_{11} & \mathbf{D}_{12} & \mathbf{0} \\ \mathbf{D}_{21} & \mathbf{D}_{22} & \mathbf{D}_{23} \\ \mathbf{0} & \mathbf{D}_{32} & \mathbf{0} \end{bmatrix} \quad \mathbf{I}^T := [-\mathbf{1}, \mathbf{0}, \mathbf{0}], \tag{13}$$

where  $\mathbf{D}$  is constant and symmetric, we obtain from (12)

$$\begin{aligned} \delta\Pi(\boldsymbol{\theta}, \delta\boldsymbol{\theta}) &= \int_{\Omega} \begin{bmatrix} \delta\boldsymbol{\varepsilon}_g \\ \delta\boldsymbol{\sigma} \\ \delta\boldsymbol{\varepsilon} \end{bmatrix}^T \begin{bmatrix} \mathbf{0} & \mathbf{1} & \mathbf{0} \\ \mathbf{1} & \mathbf{0} & \mathbf{I}^T \\ \mathbf{0} & \mathbf{I} & \mathbf{D} \end{bmatrix} \begin{bmatrix} \boldsymbol{\varepsilon}_g \\ \boldsymbol{\sigma} \\ \boldsymbol{\varepsilon} \end{bmatrix} dA \\ &\quad + \delta\Pi_{ext} = 0, \end{aligned} \tag{14}$$

which is the basic equation for the finite element approximations of the next section.

Finally we derive the Euler-Lagrange equations associated with the introduced functional. For this purpose integration by parts is applied to (9). This yields with (11)<sub>2</sub>

$$\begin{aligned} \delta\Pi(\boldsymbol{\theta}, \delta\boldsymbol{\theta}) &= \int_{\Omega} \left[ \delta\boldsymbol{\varepsilon}_1^T \left( \frac{\partial W}{\partial \boldsymbol{\varepsilon}_1} - \boldsymbol{\sigma} \right) + \delta\boldsymbol{\varepsilon}_2^T \left( \frac{\partial W}{\partial \boldsymbol{\varepsilon}_2} + \mathbf{D}_{23} \boldsymbol{\varepsilon}_3 \right) \right. \\ &\quad \left. + \delta\boldsymbol{\sigma}^T (\boldsymbol{\varepsilon}_g - \boldsymbol{\varepsilon}_1) + \delta\boldsymbol{\varepsilon}_3^T \mathbf{g} - \left( \frac{1}{j} (j \mathbf{n}^{\alpha})_{,\alpha} + \bar{\mathbf{p}} \right) \right. \\ &\quad \cdot \delta\mathbf{u} - \left( \frac{1}{j} (j \mathbf{m}^{\alpha})_{,\alpha} + \mathbf{X}_{,\alpha} \times \mathbf{n}^{\alpha} \right) \cdot \delta\boldsymbol{\varphi} \Big] dA \\ &\quad + \int_{\Gamma_{\sigma}} \{ [j (\mathbf{n}^{\alpha} \nu_{\alpha}) - \bar{\mathbf{t}}] \cdot \delta\mathbf{u} + [j (\mathbf{m}^{\alpha} \nu_{\alpha})] \cdot \delta\boldsymbol{\varphi} \} ds = 0, \end{aligned} \tag{15}$$

where  $\nu_{\alpha}$  are components of the outward normal vector on  $\Gamma_{\sigma}$  and

$$\mathbf{n}^{\alpha} := n^{\alpha\beta} \mathbf{X}_{,\beta} + q^{\alpha} \bar{\mathbf{D}} + m^{\alpha\beta} \bar{\mathbf{D}}_{,\beta} \quad \mathbf{m}^{\alpha} := \bar{\mathbf{D}} \times m^{\alpha\beta} \mathbf{X}_{,\beta}. \tag{16}$$

Applying standard arguments of variational calculus we deduce from (15) as Euler–Lagrange equations the static and geometric field equations, the constitutive equations and the constraint  $\mathbf{g} = \mathbf{0}$

$$\left. \begin{aligned} \frac{1}{j} (j \mathbf{n}^{\alpha})_{,\alpha} + \bar{\mathbf{p}} &= \mathbf{0} & \boldsymbol{\varepsilon}_g - \boldsymbol{\varepsilon}_1 &= \mathbf{0} \\ \frac{1}{j} (j \mathbf{m}^{\alpha})_{,\alpha} + \mathbf{X}_{,\alpha} \times \mathbf{n}^{\alpha} &= \mathbf{0} & \frac{\partial W}{\partial \boldsymbol{\varepsilon}_1} - \boldsymbol{\sigma} &= \mathbf{0} \\ \frac{\partial W}{\partial \boldsymbol{\varepsilon}_2} + \mathbf{D}_{23} \boldsymbol{\varepsilon}_3 &= \mathbf{0} & \mathbf{g} &= \mathbf{0} \end{aligned} \right\} \text{ in } \Omega. \tag{17}$$

Furthermore,  $\partial W / \partial \boldsymbol{\varepsilon}_2 + \mathbf{D}_{23} \boldsymbol{\varepsilon}_3 = \mathbf{0}$  describes the equilibrium of higher order stress resultants, as is shown in Sect. 3.2. Finally one obtains the static boundary conditions

$$j (\mathbf{n}^{\alpha} \nu_{\alpha}) - \bar{\mathbf{t}} = \mathbf{0} \quad j (\mathbf{m}^{\alpha} \nu_{\alpha}) = \mathbf{0} \quad \text{on } \Gamma_{\sigma}. \tag{18}$$

The equilibrium of higher order stress resultants and the constraint are further field equations in (17) in addition to the representation in [31].

### 3 Finite element formulation

#### 3.1 Interpolation in thickness direction

The finite element approximation of the warping displacements  $\tilde{\mathbf{u}} = [\tilde{u}_1, \tilde{u}_2]^T$  as are depicted in Fig. 1 is chosen as

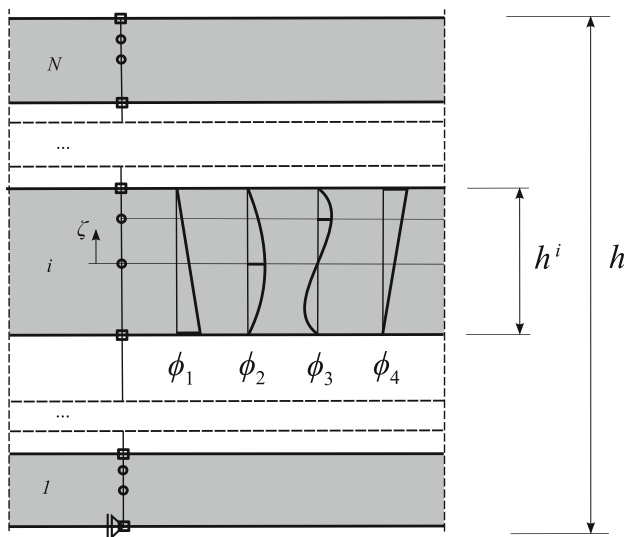


Fig. 2 Laminate with  $N$  layers

$$\tilde{\mathbf{u}}(\xi^3) = \Phi(\xi^3) \boldsymbol{\varepsilon}_2. \tag{19}$$

The vector  $\boldsymbol{\varepsilon}_2$  is elementwise constant and contains alternating the discrete warping ordinates in 1- and 2-direction of the nodes in thickness direction. Rigid body modes are avoided by suppressing the displacements of one arbitrary node, see Fig. 2. For  $N$  layers this leads to  $M = 6 \cdot N + 2$  components in  $\boldsymbol{\varepsilon}_2$ , where the first two components are zero. The interpolation matrix contains cubic hierarchic functions

$$\begin{aligned} \Phi(\xi^3) &= [\phi_1 \mathbf{1}_2 \quad \phi_2 \mathbf{1}_2 \quad \phi_3 \mathbf{1}_2 \quad \phi_4 \mathbf{1}_2] \mathbf{a}^i \\ \phi_1 &= \frac{1}{2} (1 - \zeta) \quad \phi_2 = 1 - \zeta^2 \quad \phi_3 = \frac{8}{3} \zeta (1 - \zeta^2) \\ \phi_4 &= \frac{1}{2} (1 + \zeta), \end{aligned} \tag{20}$$

where  $-1 \leq \zeta \leq 1$  is a normalized thickness coordinate of layer  $i$ . Furthermore,

$$\mathbf{a}^i = [\mathbf{0}_{8 \times 8 \cdot (i-1)} | \mathbf{1}_8 | \mathbf{0}_{8 \times (M-8-i)}]_{8 \times M} \tag{21}$$

is an assembly matrix, which relates the 8 degrees of freedom of layer  $i$  to the  $M$  components of  $\boldsymbol{\varepsilon}_2$  and  $\mathbf{1}_n$  denotes a unit matrix of order  $n$ .

Assuming orthotropic material behaviour the constitutive equations are introduced with  $S^{33} = 0$  in the following standard manner

$$\mathbf{S} = \mathbf{C} \mathbf{E}. \tag{22}$$

$$\begin{bmatrix} S^{11} \\ S^{22} \\ S^{12} \\ S^{13} \\ S^{23} \end{bmatrix} = \begin{bmatrix} C_{11} & C_{12} & C_{13} & 0 & 0 \\ C_{21} & C_{22} & C_{23} & 0 & 0 \\ C_{31} & C_{32} & C_{33} & 0 & 0 \\ 0 & 0 & 0 & C_{44} & C_{45} \\ 0 & 0 & 0 & C_{54} & C_{55} \end{bmatrix} \begin{bmatrix} E_{11} \\ E_{22} \\ 2E_{12} \\ 2E_{13} \\ 2E_{23} \end{bmatrix}$$

Due to the varying fibre orientation the material constants  $C_{ij} = C_{ji}$  differ for each individual layer. To alleviate the notation the layer index  $i$  is omitted.

The physical layer strains are obtained from

$$\mathbf{E} = [\mathbf{A}_1, \mathbf{A}_2] \begin{bmatrix} \boldsymbol{\varepsilon}_1 \\ \boldsymbol{\varepsilon}_2 \end{bmatrix} \tag{23}$$

where

$$\begin{aligned} \mathbf{A}_1 &= \begin{bmatrix} \mathbf{1}_3 & \xi^3 \mathbf{1}_3 & \mathbf{0} \\ \mathbf{0} & \mathbf{0} & \mathbf{1}_2 \end{bmatrix} \quad \mathbf{A}_2 = \begin{bmatrix} \mathbf{0}_{3 \times 8} \\ \mathbf{A}_{2s} \end{bmatrix} \mathbf{a}^i \\ \mathbf{A}_{2s} &= \frac{2}{h^i} [\phi'_1 \mathbf{1}_2 \quad \phi'_2 \mathbf{1}_2 \quad \phi'_3 \mathbf{1}_2 \quad \phi'_4 \mathbf{1}_2] \quad \phi'_j = \frac{d\phi_j}{d\zeta}. \end{aligned} \tag{24}$$

Now the relation of the stress resultants to the vector of stresses  $\mathbf{S}$  can be defined with thickness integration of the internal virtual work expression and  $\delta \mathbf{E} = \mathbf{A}_1 \delta \boldsymbol{\varepsilon}_1 + \mathbf{A}_2 \delta \boldsymbol{\varepsilon}_2$ . This yields

$$\int_{h^-}^{h^+} \delta \mathbf{E}^T \mathbf{S} \bar{\mu} d\theta^3 = \delta \boldsymbol{\varepsilon}_1^T \frac{\partial W}{\partial \boldsymbol{\varepsilon}_1} + \delta \boldsymbol{\varepsilon}_2^T \frac{\partial W}{\partial \boldsymbol{\varepsilon}_2} \tag{25}$$

with

$$\frac{\partial W}{\partial \boldsymbol{\varepsilon}_1} := \int_{h^-}^{h^+} \mathbf{A}_1^T \mathbf{S} \bar{\mu} d\theta^3 \quad \frac{\partial W}{\partial \boldsymbol{\varepsilon}_2} := \int_{h^-}^{h^+} \mathbf{A}_2^T \mathbf{S} \bar{\mu} d\theta^3, \tag{26}$$

where  $\bar{\mu}$  denotes the determinant of the shifter tensor. With an orthonormal element coordinate system, as is introduced in Sect. 3.3,  $\bar{\mu} = 1$  holds. We assert that  $\partial W / \partial \boldsymbol{\varepsilon}_2$  contains higher order stress resultants.

Furthermore, the matrices  $\mathbf{D}_{\alpha\beta}$  introduced in context with strain energy function (7)

$$W(\boldsymbol{\varepsilon}_1, \boldsymbol{\varepsilon}_2) = \frac{1}{2} \int_{h^-}^{h^+} \mathbf{E}^T \mathbf{C} \mathbf{E} \bar{\mu} d\xi^3 \quad \mathbf{E} = \sum_{\alpha=1}^2 \mathbf{A}_\alpha \boldsymbol{\varepsilon}_\alpha \tag{27}$$

can be computed by means of thickness integration. This leads to

$$\mathbf{D}_{\alpha\beta} = \int_{h^-}^{h^+} \mathbf{A}_\alpha^T \mathbf{C} \mathbf{A}_\beta \bar{\mu} d\xi^3. \tag{28}$$

Now, inserting (22) with (23) into (26) yields with (28) the constitutive law for the stress resultants (11)<sub>1</sub>.

The material matrix  $\mathbf{D}_{11}$  reads

$$\mathbf{D}_{11} = \int_{h^-}^{h^+} \mathbf{A}_1^T \mathbf{C} \mathbf{A}_1 \bar{\mu} d\xi^3 = \begin{bmatrix} \mathbf{D}_m & \mathbf{D}_{mb} & \mathbf{0} \\ \mathbf{D}_{mb}^T & \mathbf{D}_b & \mathbf{0} \\ \mathbf{0} & \mathbf{0} & \mathbf{D}_s \end{bmatrix}_{(8 \times 8)} \quad (29)$$

The submatrices for membrane, bending and shear are obtained by summation over  $N$  layers and exact integration in each layer leading to well-known expressions. For certain layer sequences the coupling matrix  $\mathbf{D}_{mb}$  vanishes. Shear correction factors, as are used in a first order shear deformation theory, are not introduced in  $\mathbf{D}_s$ .

Inserting (22) and (24) into (28) the matrices  $\mathbf{D}_{22}$  and  $\mathbf{D}_{21}$  can now be assembled with the contributions of the layers

$$\mathbf{D}_{22} = \sum_{i=1}^N \mathbf{a}^{iT} \mathbf{D}_{22}^i \mathbf{a}^i \quad \mathbf{D}_{21} = \sum_{i=1}^N \mathbf{a}^{iT} \mathbf{D}_{21}^i \quad (30)$$

where

$$\begin{aligned} \mathbf{D}_{22}^i &= \int_{-1}^{+1} \mathbf{A}_{2s}^T \mathbf{C}_s \mathbf{A}_{2s} \bar{\mu} \frac{h^i}{2} d\zeta & \mathbf{C}_s &= \begin{bmatrix} C_{44} & C_{45} \\ C_{54} & C_{55} \end{bmatrix} \\ \mathbf{D}_{21}^i &= \int_{-1}^{+1} \mathbf{A}_{2s}^T \mathbf{C}_s \mathbf{A}_{1s} \bar{\mu} \frac{h^i}{2} d\zeta & \mathbf{A}_{1s} &= [\mathbf{0}_{2 \times 6} \quad \mathbf{1}_2]. \end{aligned} \quad (31)$$

With  $\bar{\mu} = 1$  only powers of  $\zeta$  occur in (31) and analytical integration is possible. A numerical integration with 3 Gauss integration points also leads to correct results. Due to the interpolation functions with local layerwise support it follows that  $\mathbf{D}_{22}$  is sparse.

### 3.2 Equilibrium of stresses and constraint $\mathbf{g} = \mathbf{0}$

Neglecting body forces the equilibrium equations for the in-plane directions read

$$\begin{bmatrix} S^{11}_{,1} + S^{12}_{,2} + S^{13}_{,3} \\ S^{12}_{,1} + S^{22}_{,2} + S^{23}_{,3} \end{bmatrix} = \mathbf{f} = \mathbf{0}. \quad (32)$$

In (32) the bending stresses  $S^{11}$ ,  $S^{22}$ , and  $S^{12}$  as well as transverse shear stresses  $S^{13}$  and  $S^{23}$  enter. The local element coordinate system, as is introduced in Sect. 3.3, is orthogonal and constant in each element. This allows partial derivatives instead of covariant derivatives.

For the bending stresses holds with (22)

$$\begin{bmatrix} S^{11} \\ S^{22} \\ S^{12} \end{bmatrix} = \hat{\xi}^3 \begin{bmatrix} C_{11} & C_{12} & C_{13} \\ C_{21} & C_{22} & C_{23} \\ C_{31} & C_{32} & C_{33} \end{bmatrix} \begin{bmatrix} \kappa_{11} \\ \kappa_{22} \\ 2\kappa_{12} \end{bmatrix} \quad (33)$$

with  $\hat{\xi}^3 = \xi^3 - \xi_{si}^3$ , where  $\xi_{si}^3$  denotes the coordinates of the ideal centre of gravity of the laminate.

Hence, the sum of the derivatives of the bending stresses yields

$$\begin{bmatrix} S^{11}_{,1} + S^{12}_{,2} \\ S^{12}_{,1} + S^{22}_{,2} \end{bmatrix} = \hat{\xi}^3 \begin{bmatrix} C_{11} & C_{12} & C_{13} & C_{31} & C_{32} & C_{33} \\ C_{31} & C_{32} & C_{33} & C_{21} & C_{22} & C_{23} \end{bmatrix} \times \begin{bmatrix} \kappa_{11,1} \\ \kappa_{22,1} \\ 2\kappa_{12,1} \\ \kappa_{11,2} \\ \kappa_{22,2} \\ 2\kappa_{12,2} \end{bmatrix} \quad (34)$$

$$\mathbf{f}_1 = \hat{\xi}^3 \bar{\mathbf{C}}_{23} \bar{\mathbf{e}}_3$$

Within the following integrals the terms of the in-plane equilibrium are weighted with the local interpolation functions  $\Phi(\xi^3)$

$$\begin{aligned} \frac{\partial W}{\partial \mathbf{e}_2} &= - \int_{h^-}^{h^+} \Phi^T \begin{bmatrix} S^{13}_{,3} \\ S^{23}_{,3} \end{bmatrix} \bar{\mu} d\xi^3 \\ \bar{\mathbf{D}}_{23} &:= - \int_{h^-}^{h^+} \Phi^T \bar{\mathbf{C}}_{23} \hat{\xi}^3 \bar{\mu} d\xi^3. \end{aligned} \quad (35)$$

The reformulation of (26)<sub>2</sub> with  $\bar{\mu} = 1$  into (35)<sub>1</sub> is obtained with integration by parts and consideration of the stress boundary conditions  $S^{\alpha 3}(h^-) = S^{\alpha 3}(h^+) = 0$ .

The 6 columns of  $\bar{\mathbf{D}}_{23}$  are not linearly independent. For a homogeneous shell it follows immediately that the 1st, 2nd and 6th column vector are linear dependent and accordingly the 3rd, 4th and 5th column vector. Since the components of  $\bar{\mathbf{e}}_3$  still have to be determined, it is exact for homogeneous shells to reduce  $\bar{\mathbf{D}}_{23}$  to a matrix with two columns by adding the linear dependent columns. For this purpose we define

$$\begin{aligned} \mathbf{D}_{23} &= - \int_{h^-}^{h^+} \Phi^T \mathbf{C}_{23} \hat{\xi}^3 \bar{\mu} d\xi^3 \\ \mathbf{C}_{23} &= \begin{bmatrix} C_{11} + C_{12} + C_{33} & C_{13} + C_{31} + C_{32} \\ C_{31} + C_{32} + C_{23} & C_{33} + C_{21} + C_{22} \end{bmatrix}. \end{aligned} \quad (36)$$

The computation of  $\mathbf{D}_{23}$  is performed by summation over layers considering (20)

$$\mathbf{D}_{23} = - \sum_{i=1}^N \mathbf{a}^{iT} \mathbf{D}_{23}^i \quad (37)$$

where

$$\mathbf{D}_{23}^i = \int_{-1}^{+1} \boldsymbol{\phi}^{iT} \mathbf{C}_{23} \hat{\xi}^3 \bar{\mu} \frac{h^i}{2} d\xi$$

$$\boldsymbol{\phi}^i = [\phi_1 \mathbf{1}_2 \quad \phi_2 \mathbf{1}_2 \quad \phi_3 \mathbf{1}_2 \quad \phi_4 \mathbf{1}_2]. \tag{38}$$

The coordinates of the ideal centre of gravity are computed for each  $C_{\alpha\beta}$

$$\xi_{si}^3 = \frac{\int_{h^-}^{h^+} C_{\alpha\beta} \xi^3 \bar{\mu} d\xi^3}{\int_{h^-}^{h^+} C_{\alpha\beta} \bar{\mu} d\xi^3} \tag{39}$$

where  $C_{\alpha\beta}$  are the components of  $\mathbf{C}_{23}$  in (36). The integration in (38) and (39) again can be done by analytical integration or numerical Gauss integration with three integration points in each layer. For symmetric laminates and  $h^- = -h/2, h^+ = h/2$  Eq. (39) yields  $\xi_{si}^3 = 0$ .

Now the integral form of the the equilibrium  $\mathbf{f} = \mathbf{0}$  according to (32) is formed with  $\delta \tilde{\mathbf{u}} = \boldsymbol{\Phi} \delta \boldsymbol{\varepsilon}_2$ . Considering (35) and (36) it follows

$$\int_{h^-}^{h^+} \delta \tilde{\mathbf{u}}^T \mathbf{f} \bar{\mu} d\xi^3 = -\delta \boldsymbol{\varepsilon}_2^T \left( \frac{\partial W}{\partial \boldsymbol{\varepsilon}_2} + \mathbf{D}_{23} \boldsymbol{\varepsilon}_3 \right) = 0 \tag{40}$$

and with  $\delta \boldsymbol{\varepsilon}_2 \neq \mathbf{0}$  one obtains Eq. (17)<sub>3</sub>. Now  $\boldsymbol{\varepsilon}_3$  contains two components.

The derivation of the constraint  $\mathbf{g} = \mathbf{0}$  follows in an analogous way. We introduce the equilibrium of the virtual bending stresses considering the variation of (34)

$$\begin{bmatrix} \delta S^{11},_{.1} + \delta S^{12},_{.2} \\ \delta S^{12},_{.1} + \delta S^{22},_{.2} \end{bmatrix} = \delta \mathbf{f}_1 = \hat{\xi}^3 \bar{\mathbf{C}}_{23} \delta \bar{\boldsymbol{\varepsilon}}_3 = \mathbf{0} \tag{41}$$

and the integral form of  $\delta \mathbf{f}_1 = \mathbf{0}$  yields with  $\tilde{\mathbf{u}} = \boldsymbol{\Phi} \boldsymbol{\varepsilon}_2$

$$\int_{h^-}^{h^+} \delta \mathbf{f}_1^T \tilde{\mathbf{u}} \bar{\mu} d\xi^3 = \delta \bar{\boldsymbol{\varepsilon}}_3^T \int_{h^-}^{h^+} \hat{\xi}^3 \bar{\mathbf{C}}_{23}^T \boldsymbol{\Phi} \bar{\mu} d\xi^3 \boldsymbol{\varepsilon}_2 = 0. \tag{42}$$

With the reduced matrix  $\mathbf{C}_{23}$  according to (36) we define

$$\mathbf{D}_{32} = - \int_{h^-}^{h^+} \mathbf{C}_{23}^T \boldsymbol{\Phi} \hat{\xi}^3 \bar{\mu} d\xi^3 = \mathbf{D}_{23}^T \tag{43}$$

with now two rows. From (42) considering (43) follows  $\delta \boldsymbol{\varepsilon}_3^T \mathbf{D}_{32} \boldsymbol{\varepsilon}_2 = 0$  and with  $\delta \boldsymbol{\varepsilon}_3 \neq \mathbf{0}$  one obtains the constraint (8). It has the descriptive meaning that the warping

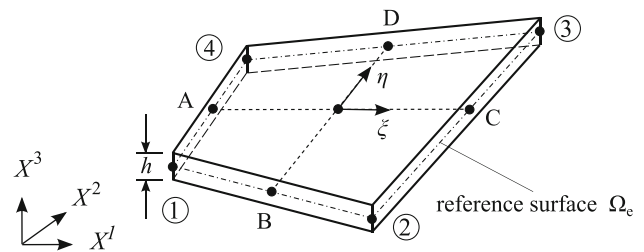


Fig. 3 Quadrilateral shell element

displacements must not lead to additional bending moments as is illustrated in Fig. 1.

*Remark* For inhomogeneous shells the procedure to add the quasi linear dependent columns represents an approximation. However, in our numerical tests we obtain good agreement with costly three-dimensional solutions. With an increasing number of layers differences to the reference solution practically vanish. This can be observed with the examples in Sect. 4.2. For homogeneous shells the approach is exact.

### 3.3 Approximation of the independent fields

In this section the finite element shape functions for quadrilaterals are specified applying the isoparametric concept. The numbering of the corner nodes and midside nodes can be seen in Fig. 3.

A map of the coordinates  $\{\xi, \eta\} \in [-1, 1]$  from the unit square to the reference surface is applied. Hence position vector and director vector of the reference surface are interpolated with bi-linear shape functions

$$\mathbf{X}^h = \sum_{I=1}^4 N_I \mathbf{X}_I \quad \bar{\mathbf{D}}^h = \sum_{I=1}^4 N_I \bar{\mathbf{D}}_I, \tag{44}$$

where  $N_I(\xi, \eta) = \frac{1}{4}(1 + \xi_I \xi)(1 + \eta_I \eta)$  with  $\xi_I \in \{-1, 1, 1, -1\}, \eta_I \in \{-1, -1, 1, 1\}$  and superscript  $h$  refers to the finite element approximation.

The position vectors  $\mathbf{X}_I$  and the orthonormal basis systems  $[\mathbf{A}_{1I}, \mathbf{A}_{2I}, \mathbf{A}_{3I}]$  at the nodes are generated within the mesh input. Here,  $\bar{\mathbf{D}}_I = \mathbf{A}_{3I}$  is perpendicular to  $\Omega$  and  $\mathbf{A}_{1I}, \mathbf{A}_{2I}$  are constructed in such a way that boundary conditions can be accommodated.

The tangent vectors  $\mathbf{X}^h_{, \alpha}$  and the derivatives of the director field  $\bar{\mathbf{D}}^h_{, \alpha}$  are computed as follows

$$\mathbf{X}^h_{, \alpha} = \sum_{I=1}^4 N_{I, \alpha} \mathbf{X}_I \quad \bar{\mathbf{D}}^h_{, \alpha} = \sum_{I=1}^4 N_{I, \alpha} \bar{\mathbf{D}}_I. \tag{45}$$

The derivatives of the shape functions are obtained with the inverse of Jacobian matrix  $\mathbf{J}$

$$\begin{bmatrix} N_{I,1} \\ N_{I,2} \end{bmatrix} = \mathbf{J}^{-1} \begin{bmatrix} N_{I,\xi} \\ N_{I,\eta} \end{bmatrix} \quad \mathbf{J} = \begin{bmatrix} \mathbf{X}^h_{,\xi} \cdot \mathbf{t}_1 & \mathbf{X}^h_{,\xi} \cdot \mathbf{t}_2 \\ \mathbf{X}^h_{,\eta} \cdot \mathbf{t}_1 & \mathbf{X}^h_{,\eta} \cdot \mathbf{t}_2 \end{bmatrix} \quad (46)$$

where  $\mathbf{X}^h_{,\xi}$  and  $\mathbf{X}^h_{,\eta}$  are computed replacing  $N_I$  by  $N_{I,\xi}$  and  $N_{I,\eta}$  in (44)<sub>1</sub>. Furthermore,  $\mathbf{t}_i$  denotes the element coordinate system with  $\mathbf{t}_i \cdot \mathbf{t}_j = \delta_{ij}$ , see [31]. The vectors  $\mathbf{t}_1$  and  $\mathbf{t}_2$  span a tangent plane at the centre of the element and  $\mathbf{t}_3$  is normal vector.

The displacements and rotations of the reference surface are approximated with the same interpolation functions

$$\mathbf{u}^h = \sum_{I=1}^4 N_I \mathbf{u}_I \quad \Delta \mathbf{d}^h = \sum_{I=1}^4 N_I \Delta \mathbf{d}_I \quad (47)$$

The derivatives  $\mathbf{u}^h_{,\alpha}$  and  $\Delta \mathbf{d}^h_{,\alpha}$  are obtained in a corresponding way according to (45).

Here,  $\mathbf{u}_I = u_{Ik} \mathbf{e}_k$  describes the nodal displacement vector. With  $\bar{\mathbf{D}}_I = \bar{D}_{Ik} \mathbf{e}_k$  holds

$$\Delta \mathbf{d}_I = \boldsymbol{\varphi}_I \times \bar{\mathbf{D}}_I = \mathbf{W}_I^T \boldsymbol{\varphi}_I \quad \mathbf{W}_I = \begin{bmatrix} 0 & -\bar{D}_{I3} & \bar{D}_{I2} \\ \bar{D}_{I3} & 0 & -\bar{D}_{I1} \\ -\bar{D}_{I2} & \bar{D}_{I1} & 0 \end{bmatrix} \quad (48)$$

At nodes which are not positioned on intersections a drilling stiffness is not available and a transformation of the rotation vector to the nodal coordinate system is necessary:

$$\begin{aligned} \boldsymbol{\varphi}_I &= \mathbf{T}_{3I} \boldsymbol{\beta}_I \\ \mathbf{T}_{3I} &= \begin{cases} \mathbf{1}_3 & \text{for nodes on shell intersections} \\ [\mathbf{A}_{1I}, \mathbf{A}_{2I}]_{(3 \times 2)} & \text{for all other nodes} \end{cases} \\ \boldsymbol{\beta}_I &= \begin{cases} [\beta_{xI}, \beta_{yI}, \beta_{zI}]^T & \text{for nodes on shell intersections} \\ [\beta_{1I}, \beta_{2I}]^T & \text{for all other nodes} \end{cases} \end{aligned} \quad (49)$$

Here,  $\beta_{\alpha I}$  are the rotations about local axes defined by  $\mathbf{A}_{\alpha I}$ . The drilling degree of freedom is fixed, thus  $\beta_{3I} = 0$ . Next combining (48) and (49) one obtains

$$\Delta \mathbf{d}_I = \mathbf{T}_I \boldsymbol{\beta}_I \quad \mathbf{T}_I = \mathbf{W}_I^T \mathbf{T}_{3I} \quad (50)$$

The element has to fulfil membrane and bending patch test. The bending patch test—when using below specified mixed interpolation—can be fulfilled with substitute shear strains introduced e.g. in Ref. [33], but not with the transverse shear

strains (3)<sub>3</sub>. Thus, the finite element approximation of the shell strains (3) reads

$$\boldsymbol{\varepsilon}_g^h = \begin{bmatrix} \varepsilon_{11}^h \\ \varepsilon_{22}^h \\ 2\varepsilon_{12}^h \\ \kappa_{11}^h \\ \kappa_{22}^h \\ 2\kappa_{12}^h \\ \gamma_1^h \\ \gamma_2^h \end{bmatrix} = \begin{bmatrix} \mathbf{u}^h_{,1} \cdot \mathbf{X}^h_{,1} \\ \mathbf{u}^h_{,2} \cdot \mathbf{X}^h_{,2} \\ \mathbf{u}^h_{,1} \cdot \mathbf{X}^h_{,2} + \mathbf{u}^h_{,2} \cdot \mathbf{X}^h_{,1} \\ \mathbf{u}^h_{,1} \cdot \bar{\mathbf{D}}^h_{,1} + \mathbf{X}^h_{,1} \cdot \Delta \mathbf{d}^h_{,1} \\ \mathbf{u}^h_{,2} \cdot \bar{\mathbf{D}}^h_{,2} + \mathbf{X}^h_{,2} \cdot \Delta \mathbf{d}^h_{,2} \\ \mathbf{u}^h_{,1} \cdot \bar{\mathbf{D}}^h_{,2} + \mathbf{u}^h_{,2} \cdot \bar{\mathbf{D}}^h_{,1} + \mathbf{X}^h_{,1} \cdot \Delta \mathbf{d}^h_{,2} + \mathbf{X}^h_{,2} \cdot \Delta \mathbf{d}^h_{,1} \\ \mathbf{J}^{-1} \left\{ \begin{array}{l} \frac{1}{2}[(1-\eta)\gamma_\xi^B + (1+\eta)\gamma_\xi^D] \\ \frac{1}{2}[(1-\xi)\gamma_\eta^A + (1+\xi)\gamma_\eta^C] \end{array} \right\} \end{bmatrix} \quad (51)$$

The shear strains  $\gamma_\xi^M$  and  $\gamma_\eta^L$  at the midside nodes  $M = B, D$  and  $L = A, C$  are specified in Appendix 2.

Inserting above finite element approximations into the shell strains (51) yields

$$\boldsymbol{\varepsilon}_g^h = \mathbf{B} \hat{\mathbf{v}} \quad (52)$$

where  $\mathbf{B}$  is given in Appendix 2 and  $\hat{\mathbf{v}} = [\mathbf{v}_1, \mathbf{v}_2, \mathbf{v}_3, \mathbf{v}_4]^T$  is the element displacement vector with  $\mathbf{v}_I = [\mathbf{u}_I, \boldsymbol{\beta}_I]^T$ .

The independent stress resultants  $\boldsymbol{\sigma}$  are approximated as follows

$$\boldsymbol{\sigma}^h = \mathbf{N}_\sigma \hat{\boldsymbol{\sigma}} \quad (53)$$

where  $\hat{\boldsymbol{\sigma}}$  contains 8 parameters for the constant part and 6 parameters for the varying part of the stress field, respectively.

The approximation of  $\boldsymbol{\varepsilon}$  consists of three parts

$$\begin{bmatrix} \boldsymbol{\varepsilon}_1 \\ \boldsymbol{\varepsilon}_2 \\ \boldsymbol{\varepsilon}_3 \end{bmatrix} = \begin{bmatrix} \mathbf{N}_\varepsilon^1 & \mathbf{0} & \mathbf{0} \\ \mathbf{0} & \mathbf{1} & \mathbf{0} \\ \mathbf{0} & \mathbf{0} & \mathbf{1} \end{bmatrix} \begin{bmatrix} \hat{\boldsymbol{\varepsilon}}_1 \\ \hat{\boldsymbol{\varepsilon}}_2 \\ \hat{\boldsymbol{\varepsilon}}_3 \end{bmatrix} \quad (54)$$

$$\boldsymbol{\varepsilon}^h = \mathbf{N}_\varepsilon \hat{\boldsymbol{\varepsilon}}.$$

The first part with 14 parameters and interpolation matrix  $\mathbf{N}_\varepsilon^1$  corresponds to (53). The second and third part are chosen constant within the element. The matrices  $\mathbf{N}_\sigma$  and  $\mathbf{N}_\varepsilon^1$  are specified in Appendix 2.



### 3.4 Element stiffness matrix

The approximations (52)–(54) and the corresponding equations for the virtual quantities

$$\begin{aligned} \boldsymbol{\theta}^h &:= \begin{bmatrix} \boldsymbol{\varepsilon}_g^h \\ \boldsymbol{\sigma}^h \\ \boldsymbol{\varepsilon}^h \end{bmatrix} = \begin{bmatrix} \mathbf{B} & \mathbf{0} & \mathbf{0} \\ \mathbf{0} & \mathbf{N}_\sigma & \mathbf{0} \\ \mathbf{0} & \mathbf{0} & \mathbf{N}_\varepsilon \end{bmatrix} \begin{bmatrix} \hat{\mathbf{v}} \\ \hat{\boldsymbol{\sigma}} \\ \hat{\boldsymbol{\varepsilon}} \end{bmatrix} \\ \delta\boldsymbol{\theta}^h &:= \begin{bmatrix} \delta\boldsymbol{\varepsilon}_g^h \\ \delta\boldsymbol{\sigma}^h \\ \delta\boldsymbol{\varepsilon}^h \end{bmatrix} = \begin{bmatrix} \mathbf{B} & \mathbf{0} & \mathbf{0} \\ \mathbf{0} & \mathbf{N}_\sigma & \mathbf{0} \\ \mathbf{0} & \mathbf{0} & \mathbf{N}_\varepsilon \end{bmatrix} \begin{bmatrix} \delta\hat{\mathbf{v}} \\ \delta\hat{\boldsymbol{\sigma}} \\ \delta\hat{\boldsymbol{\varepsilon}} \end{bmatrix} \end{aligned} \quad (55)$$

are inserted into the finite element approximation of (14)

$$\begin{aligned} \delta\Pi(\boldsymbol{\theta}^h, \delta\boldsymbol{\theta}^h) &= \sum_{e=1}^{numel} \left\{ \int_{\Omega_e} \begin{bmatrix} \delta\boldsymbol{\varepsilon}_g^h \\ \delta\boldsymbol{\sigma}^h \\ \delta\boldsymbol{\varepsilon}^h \end{bmatrix}^T \begin{bmatrix} \mathbf{0} & \mathbf{1} & \mathbf{0} \\ \mathbf{1} & \mathbf{0} & \mathbf{I}^T \\ \mathbf{0} & \mathbf{I} & \mathbf{D} \end{bmatrix} \begin{bmatrix} \boldsymbol{\varepsilon}_g^h \\ \boldsymbol{\sigma}^h \\ \boldsymbol{\varepsilon}^h \end{bmatrix} dA + \delta\Pi_{ext}^{eh} \right\} = 0, \end{aligned} \quad (56)$$

where *numel* denotes the total number of finite shell elements to discretise the problem. Furthermore,  $\delta\Pi_{ext}^{eh} = -\delta\hat{\mathbf{v}}^T \mathbf{f}_{ext}$ , where  $\mathbf{f}_{ext}$  corresponds to the vector of loads  $\bar{\mathbf{p}}$  and  $\bar{\mathbf{t}}$  of a standard displacement formulation. Thus, Eq. (56) yields with (55)

$$\begin{aligned} \delta\Pi(\boldsymbol{\theta}^h, \delta\boldsymbol{\theta}^h) &= \sum_{e=1}^{numel} \begin{bmatrix} \delta\hat{\mathbf{v}} \\ \delta\hat{\boldsymbol{\sigma}} \\ \delta\hat{\boldsymbol{\varepsilon}} \end{bmatrix}^T \\ &\times \left\{ \begin{bmatrix} \mathbf{0} & \mathbf{G}^T & \mathbf{0} \\ \mathbf{G} & \mathbf{0} & \mathbf{F}^T \\ \mathbf{0} & \mathbf{F} & \mathbf{H} \end{bmatrix} \begin{bmatrix} \hat{\mathbf{v}} \\ \hat{\boldsymbol{\sigma}} \\ \hat{\boldsymbol{\varepsilon}} \end{bmatrix} - \begin{bmatrix} \mathbf{f}_{ext} \\ \mathbf{0} \\ \mathbf{0} \end{bmatrix} \right\} = 0 \end{aligned} \quad (57)$$

with

$$\begin{aligned} \mathbf{F} &= \int_{\Omega_e} \mathbf{N}_\varepsilon^T \mathbf{I} \mathbf{N}_\sigma dA & \mathbf{G} &= \int_{\Omega_e} \mathbf{N}_\sigma^T \mathbf{B} dA \\ \mathbf{H} &= \int_{\Omega_e} \mathbf{N}_\varepsilon^T \mathbf{D} \mathbf{N}_\varepsilon dA. \end{aligned} \quad (58)$$

The integrals in (58) are computed numerically using a  $2 \times 2$  Gauss integration scheme.

For each element one obtains the set of equations

$$\begin{aligned} \mathbf{G}^T \hat{\boldsymbol{\sigma}} - \mathbf{f}_{ext} &= \mathbf{r} \\ \mathbf{G} \hat{\mathbf{v}} + \mathbf{F}^T \hat{\boldsymbol{\varepsilon}} &= \mathbf{0} \\ \mathbf{F} \hat{\boldsymbol{\sigma}} + \mathbf{H} \hat{\boldsymbol{\varepsilon}} &= \mathbf{0}, \end{aligned} \quad (59)$$

where  $\mathbf{r}$  denotes the vector of element nodal forces which cancels out with the assembly. Since  $\boldsymbol{\sigma}$  and  $\boldsymbol{\varepsilon}$  are interpolated

discontinuously across the element boundaries the parameters  $\hat{\boldsymbol{\varepsilon}}$  and  $\hat{\boldsymbol{\sigma}}$  can be eliminated from (59)

$$\begin{aligned} \hat{\boldsymbol{\varepsilon}} &= -\mathbf{H}^{-1} \mathbf{F} \hat{\boldsymbol{\sigma}} \\ \hat{\boldsymbol{\sigma}} &= \hat{\mathbf{H}} \mathbf{G} \hat{\mathbf{v}} \quad \hat{\mathbf{H}} = (\mathbf{F}^T \mathbf{H}^{-1} \mathbf{F})^{-1}. \end{aligned} \quad (60)$$

Inserting  $\hat{\boldsymbol{\sigma}}$  from (60) in Eq. (57) yields  $\delta\Pi(\boldsymbol{\theta}^h, \delta\boldsymbol{\theta}^h) = \sum_{e=1}^{numel} \delta\hat{\mathbf{v}}^T (\mathbf{K} \hat{\mathbf{v}} - \mathbf{f}_{ext}) = 0$  with

$$\mathbf{K} = \mathbf{G}^T \hat{\mathbf{H}} \mathbf{G}. \quad (61)$$

The element stiffness matrix  $\mathbf{K}$  possesses with six zero eigenvalues the correct rank. The global system of equations is obtained by standard assembly procedures. At nodes on intersections there are six degrees of freedom (three displacements and three global rotations) and five at all other nodes (three displacements and two local rotations). The solution yields the global displacement vector and thus for each element the vector  $\hat{\mathbf{v}}$ . For the back substitution of  $\hat{\boldsymbol{\sigma}}$  and  $\hat{\boldsymbol{\varepsilon}}$  according to (60) the necessary matrices have to be stored or to be recalculated.

*Remark* Due to the special structure of matrix

$$\mathbf{F} = \begin{bmatrix} \mathbf{F}_1 \\ \mathbf{0} \end{bmatrix} \quad \mathbf{F}_1 = - \int_{\Omega_e} \mathbf{N}_\varepsilon^{1T} \mathbf{N}_\sigma dA, \quad (62)$$

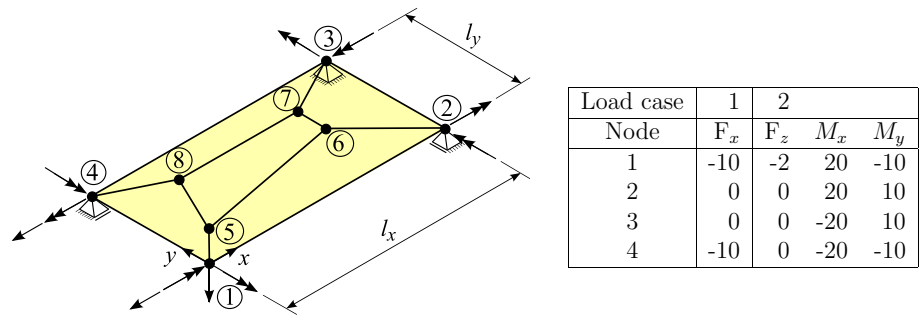
where  $\mathbf{F}_1$  is regular and sparse, the two matrix inversions in  $\hat{\mathbf{H}} = (\mathbf{F}^T \mathbf{H}^{-1} \mathbf{F})^{-1}$  according to (60) are not necessary. In stead of this a static condensation of the parameters  $\boldsymbol{\varepsilon}_2$  and  $\boldsymbol{\varepsilon}_3$  in (59) is more effective, see [32]. This leads to

$$\hat{\mathbf{H}} = \mathbf{F}_1^{-1} \hat{\mathbf{H}}_{11} \mathbf{F}_1^{-T} \quad \hat{\mathbf{H}}_{11} = \mathbf{H}_{11} - \mathbf{H}_{12} \mathbf{H}_{22}^{-1} \mathbf{H}_{21} \quad (63)$$

with  $\mathbf{H}_{\alpha\beta} = \int_{\Omega_e} \mathbf{N}_\varepsilon^{\alpha T} \hat{\mathbf{D}}_{\alpha\beta} \mathbf{N}_\varepsilon^\beta dA$  where  $\alpha, \beta = 1, 2$ . Furthermore  $\mathbf{N}_\varepsilon^2 = \mathbf{1}$  holds and  $\hat{\mathbf{D}}_{\alpha\beta}$  denote submatrices of matrix  $\mathbf{D}$ . The computation of  $\mathbf{F}_1^{-1}$  requires the inversion of a diagonal submatrix and of three  $2 \times 2$  submatrices. Furthermore a pivot change in  $\mathbf{D}$  is necessary. In fact for the programming the sequence of  $\boldsymbol{\varepsilon}_2$  and  $\boldsymbol{\varepsilon}_3$  is interchanged in the vector  $\boldsymbol{\varepsilon}$ . Due to the interpolation in thickness direction with local layerwise support the matrix  $\mathbf{H}_{22}$  is sparse which means for examples with many layers a significantly reduced effort.

The developed 4-node shell element has been implemented in an extended version of the general finite element program FEAP [34].

**Fig. 4** Rectangular plate, patch of 5 elements



**4 Examples**

For all examples with fibre reinforced polymer layers transversal isotropic material behaviour is assumed as special case of orthotropy. The material constants are chosen as

$$\begin{aligned}
 E_1 &= 125000 \text{ N/mm}^2 & G_{12} &= 4800 \text{ N/mm}^2 \\
 E_2 &= 7400 \text{ N/mm}^2 & G_{23} &= 2700 \text{ N/mm}^2 \\
 \nu_{12} &= 0.34,
 \end{aligned}
 \tag{64}$$

where the index 1 refers to the preferred direction of the material.

For the output the transverse shear stresses are evaluated via Eqs. (22) and (23) at the element centre. For comparison 8-noded solid shell elements according to Ref. [29] are used. Here, results are obtained at nodes of the global FE-mesh using a standard smoothing procedure. Due to the applied assumed strain interpolation for the transverse shear strains [33] these elements possess an orientation which must coincide with the thickness direction of the shell. Furthermore, 5 parameters are used for the enhanced strain interpolation. A relative fine discretisation for each layer is necessary to obtain sufficient accurate results for the distribution of the transverse shear stresses through the thickness. We choose 10 elements in thickness direction of each layer.

*Remark* For all examples with a layered setup holds: With the present element formulation continuity of the transverse shear stresses at the layer boundaries is automatically obtained. We do not apply any smoothing technique. At the outer surfaces the zero stress boundary conditions are fulfilled in an exact way. The integrals of the shear stress distribution coincide identically with the independently interpolated stress resultants  $q^1$  and  $q^2$ .

**4.1 Membrane and bending patch test**

At first we investigate the element performance within membrane and bending patch test as is depicted in Fig. 4, see also Ref. [35]. A rectangular plate of length  $l_x = 40$ , width  $l_y = 20$  and thickness  $h = 0.1$  is supported at three corners. The linear elastic material behaviour is described by

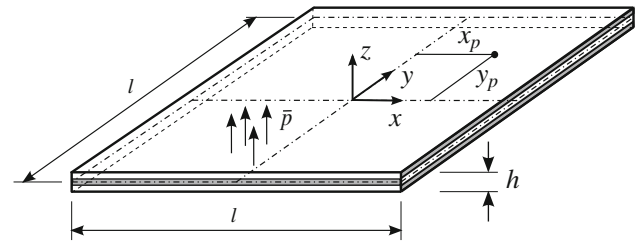


**Fig. 5** Simply supported layered plate

**Table 1** Plate with 5 different layer sequences

Plate	Layer sequence
1	$[0^\circ/90^\circ/0^\circ]$
2	$[0^\circ/90^\circ]$
3	$[45^\circ/-45^\circ/45^\circ]$
4	$[45^\circ/-45^\circ/45^\circ/-45^\circ]_s$
5	$[-45^\circ/45^\circ/-45^\circ/45^\circ/-45^\circ/45^\circ/-45^\circ/45^\circ/-45^\circ/0^\circ]_s$

$E = 10^6$  and  $\nu = 0.3$ . We consider in-plane loading and bending loading denoted by load case 1 and 2, respectively. Both, membrane and bending patch test are fulfilled by the present element. One obtains constant normal forces  $n_x = 1$ ,  $n_y = n_{xy} = 0$  (load case 1) and constant bending moments  $m_x = m_y = m_{xy} = 1$  (load case 2).

**4.2 Simply supported plate subjected to constant loading**

With the next example a square plate according to Fig. 5 is considered. The geometrical data are:  $l = 50$  mm and  $h = 1$  mm. The origin of the  $x, y, z$ -coordinate system coincides with the plate centre. The plate is simply supported (soft support) and subjected to a constant load  $\bar{p} = 1\text{N/mm}^2$ . For the discretisation with solid shell elements the loading is also applied at the middle surface. We investigate five different layer sequences as are displayed in Table 1. The fibre direction  $0^\circ$  coincides with the  $x$ -direction. A subscript  $s$  refers to symmetry of the total lay-up. Furthermore,  $(x_p, y_p)$  represent coordinates of a chosen element centre, where warping displacements or stresses are evaluated as function of the

**Table 2** Maximum displacements of the simply supported plate in [mm]

Plate	Present	Element [32]	Solid shell [29]
1	7.744	7.744	7.754
2	16.490	16.490	16.500
3	7.266	7.264	7.265
4	5.159	5.159	5.153
5	4.967	4.966	4.957

thickness coordinate. These values are specified in the respective captions of Figures.

First we compare the maximum displacements  $u_z$  at the plate centre computed with the developed element and two comparative elements. The results in Table 2 represent converged values. There is good agreement between the different models.

#### 4.2.1 Symmetric cross-ply laminate

At first a symmetric cross-ply laminate  $[0^\circ/90^\circ/0^\circ]$  is investigated. The applied discretisations for both models using regular meshes and the coordinates of the stress evaluation are given in Figs. 7 and 8.

The shape of the normalized warping displacement

$$\hat{u}_x = \tilde{u}_x - \frac{1}{h} \int_{-h/2}^{+h/2} \tilde{u}_x dz \tag{65}$$

at the specified coordinates computed with the developed element is shown in Fig. 6. One can see the typical shape as is qualitatively depicted for a homogeneous shell in Fig. 1b. The transverse shear stresses according to Figs. 7 and 8 show good correlation between the two applied models, see Tables 3 and 4.

**Fig. 6**  $\hat{u}_x(x_p = 21.429 \text{ mm}, y_p = 0, z)$  for a cross-ply laminate  $[0^\circ/90^\circ/0^\circ]$

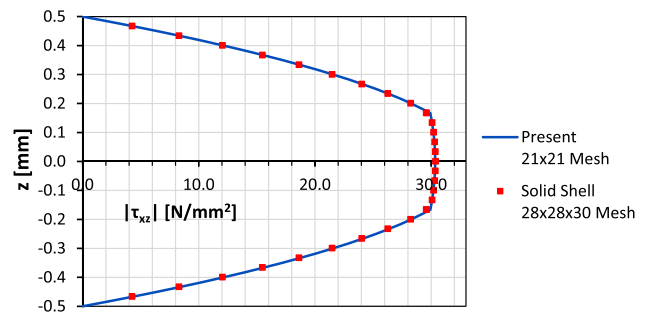
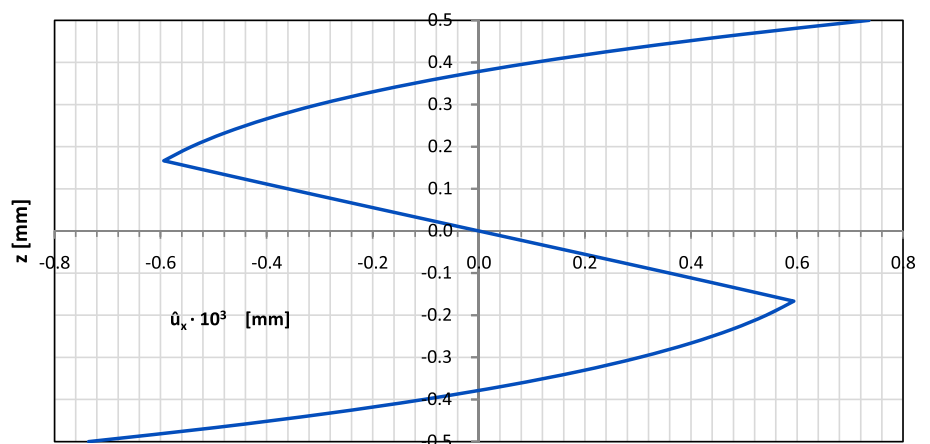


**Fig. 7**  $\tau_{xz}(x_p = 21.429 \text{ mm}, y_p = 0, z)$  for a cross-ply laminate  $[0^\circ/90^\circ/0^\circ]$

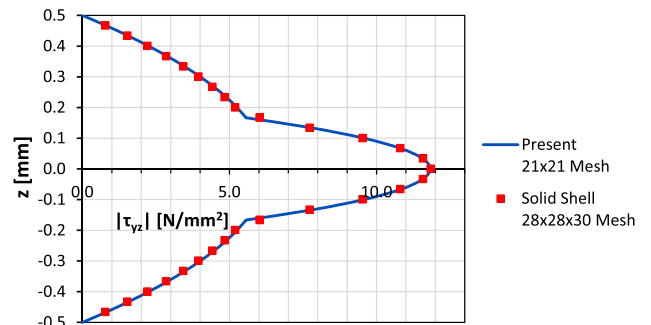


**Fig. 8**  $\tau_{yz}(x_p = 0, y_p = 21.429 \text{ mm}, z)$  for a cross-ply laminate  $[0^\circ/90^\circ/0^\circ]$

The influence of mesh distortion on the results has also been investigated. We compare results for  $\tau_{xz}(z = 0)$  of a distorted mesh (1594 elements, 1675 nodes-generated with a meshing scheme based on an advancing front technique) with a regular mesh (1600 elements, 1681 nodes) for a quarter of the plate. Figures 9 and 10 show that only negligible differences occur when a distorted mesh is used.

#### 4.2.2 Unsymmetric cross-ply laminate

Here we consider the unsymmetric cross-ply laminate  $[0^\circ/90^\circ]$ . The discretisation density for the respective model

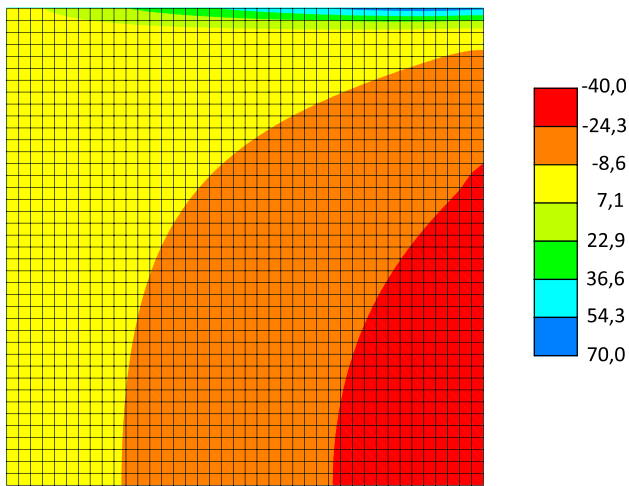


**Fig. 9**  $\tau_{xz}(x, y, z = 0)$  in  $\text{N/mm}^2$  for lay-up  $[0^\circ/90^\circ/0^\circ]$  using a regular mesh

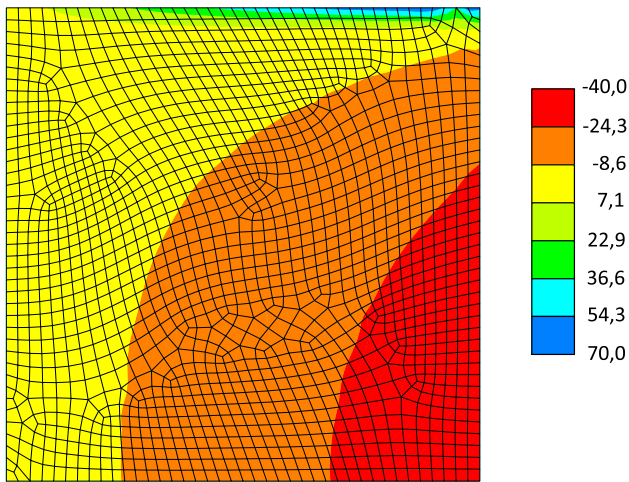


**Fig. 10**  $\tau_{xz}(x, y, z = 0)$  in  $\text{N/mm}^2$  for lay-up  $[0^\circ/90^\circ/0^\circ]$  using a distorted mesh

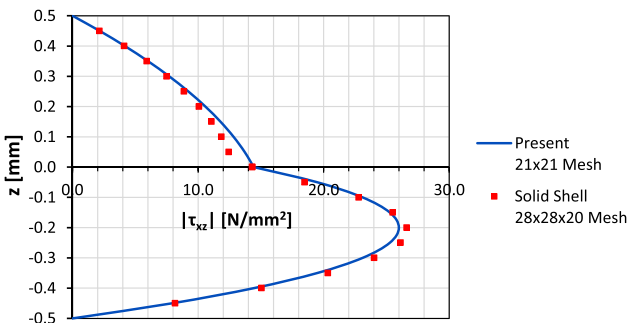


**Fig. 11**  $\tau_{xz}(x_p = 21.429 \text{ mm}, y_p = 0, z)$  for an unsymmetric lay-up  $[0^\circ/90^\circ]$

applying regular meshes and the coordinates of the stress evaluation are given in Figs. 11 and 12. The results for the shear stresses computed with the two models show only small differences, see also Table 5.

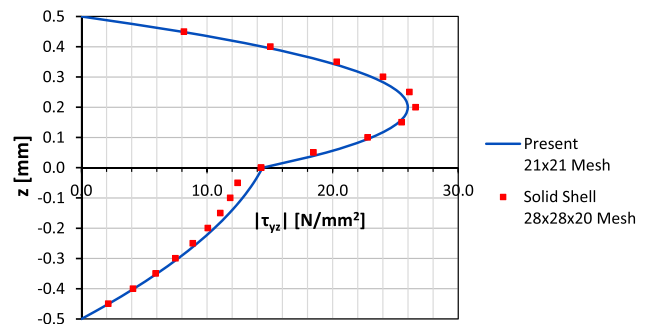


**Fig. 12**  $\tau_{yz}(x_p = 0, y_p = 21.429 \text{ mm}, z)$  for an unsymmetric lay-up  $[0^\circ/90^\circ]$

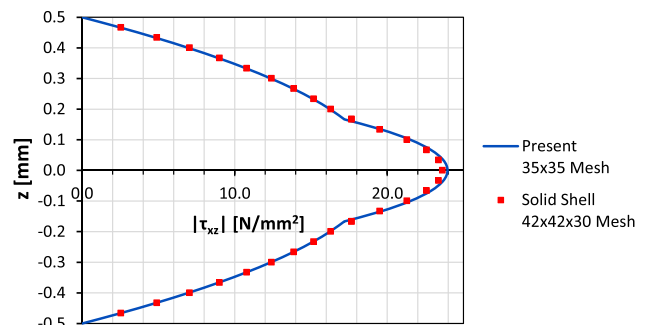


**Fig. 13**  $\tau_{xz}(x_p = 21.429 \text{ mm}, y_p = 0, z)$  for an angle ply lay-up  $[45^\circ/-45^\circ/45^\circ]$

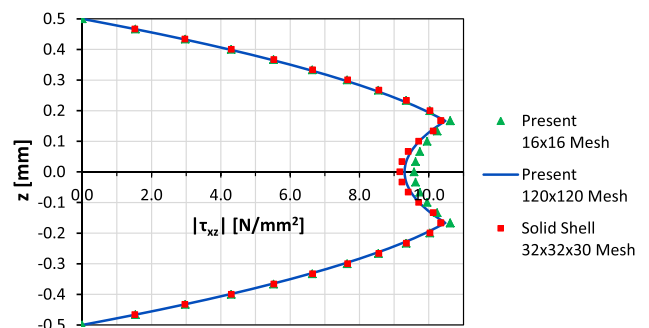


**Fig. 14**  $\tau_{xz}(x_p = 10.937 \text{ mm}, y_p = 14.062 \text{ mm}, z)$  for an angle ply lay-up  $[45^\circ/-45^\circ/45^\circ]$

### 4.2.3 Angle-ply laminate with 3 layers

The angle ply lay-up  $[45^\circ/-45^\circ/45^\circ]$  is considered next. The applied discretisations using regular meshes for the two models and the coordinates of the stress evaluation are given in Figs. 13, 14, and 15. The shape of  $\tau_{yz}(x_p = 0, y_p = 21.429 \text{ mm}, z)$  corresponds to the distribution of  $\tau_{xz}$  in Fig. 13, and therefore is not displayed. Instead of this we present the stress evaluation at the coordinates given in Fig. 14. It shows the interesting effect that a drop of  $\tau_{xz}$  in the middle layer takes place. The evaluation of  $\tau_{yz}$  at the same coordinates yields a distribution as in a homogeneous plate, Fig. 15. Discrete data are presented in Tables 6–8.

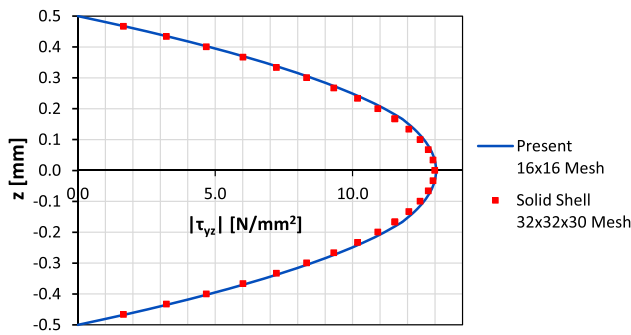


**Fig. 15**  $\tau_{yz}(x_p = 10.937 \text{ mm}, y_p = 14.062 \text{ mm}, z)$  for an angle ply lay-up  $[45^\circ/-45^\circ/45^\circ]$

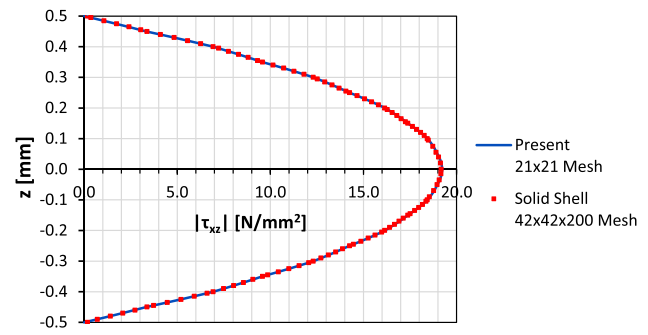


**Fig. 18**  $\tau_{xz}(x_p = 21.429 \text{ mm}, y_p = 0, z)$  for a 20 layer angle-ply laminate

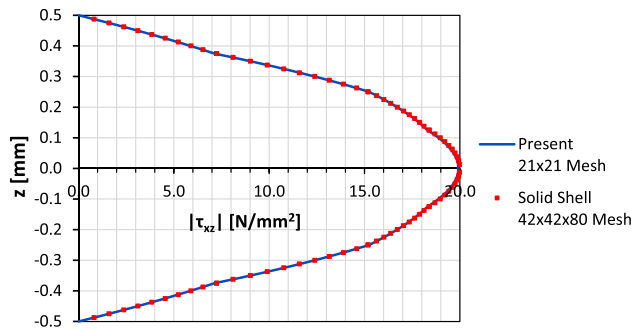


**Fig. 16**  $\tau_{xz}(x_p = 21.429 \text{ mm}, y_p = 0, z)$  for an angle ply lay-up  $[45^\circ/-45^\circ/45^\circ/-45^\circ]_s$

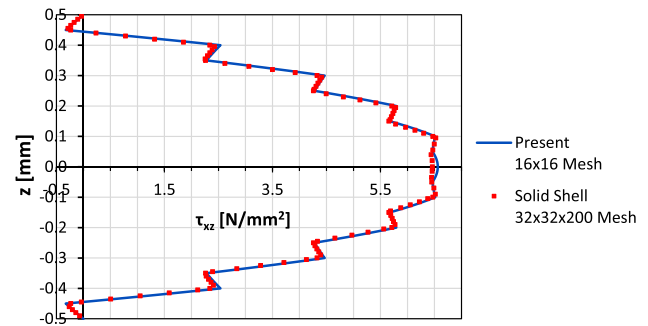


**Fig. 19**  $\tau_{xz}(x_p = 10.937 \text{ mm}, y_p = 14.062 \text{ mm}, z)$  for a 20 layer angle-ply laminate

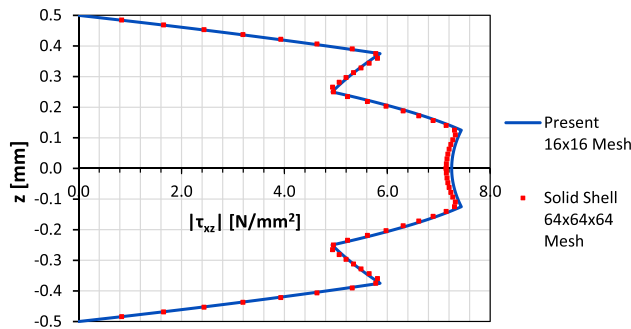


**Fig. 17**  $\tau_{xz}(x_p = 10.937 \text{ mm}, y_p = 14.062 \text{ mm}, z)$  for an angle ply lay-up  $[45^\circ/-45^\circ/45^\circ/-45^\circ]_s$

#### 4.2.4 Angle-ply laminate with 8 layers

We consider an 8 layer laminate  $[45^\circ/-45^\circ/45^\circ/-45^\circ]_s$ . The applied shell and solid shell discretisations using regular meshes can be seen in Figs. 16 and 17. The coordinates  $(x_p, y_p)$  for the evaluation of  $\tau_{xz}$  are chosen as in the previous example. In both diagrams there is good agreement of the shear stresses computed with the two models.

#### 4.2.5 Angle-ply laminate with 20 layers

Finally a 20 layer laminate  $[-45^\circ/45^\circ/-45^\circ/45^\circ/-45^\circ/45^\circ/-45^\circ/45^\circ/-45^\circ/0^\circ]_s$  is investigated. The applied shell

and solid shell discretisations using regular meshes can be seen in Figs. 18 and 19. The coordinates  $(x_p, y_p)$  for the evaluation of  $\tau_{xz}$  are chosen as in the previous example. Both diagrams show good agreement between the shear stresses of the two models.

### 4.3 Stiffened cylindrical shell

The last example represents a stiffened cylindrical shell. Figure 20 shows a cross-section of the structure and a coarse finite element mesh of half the structure considering symmetry conditions. Radius and length of the cylinder are  $R = 1000 \text{ mm}$ ,  $L = 2000 \text{ mm}$  and the shell thickness is  $h = 10 \text{ mm}$ . The shell is free at  $y = z = 0$  and clamped at  $y = L$ . A concentrated force  $F = 1 \text{ kN}$  acts at the coordinates  $(x, y, z) = (0, 0, R)$ . The skin of the structure consists of a  $[0^\circ/90^\circ/0^\circ]$  lay-up, where  $0^\circ$  refers to the tangential direction and  $90^\circ$  to the length direction of the cylinder. The stiffeners with geometrical data  $d = 50 \text{ mm}$  and  $h = 10 \text{ mm}$  are arranged in radial direction. The stiffener in the symmetry axis has a thickness of  $2h$ . The stiffeners are homogeneous and the fibre direction coincides with the length direction. Again the data for transversal isotropic material behaviour

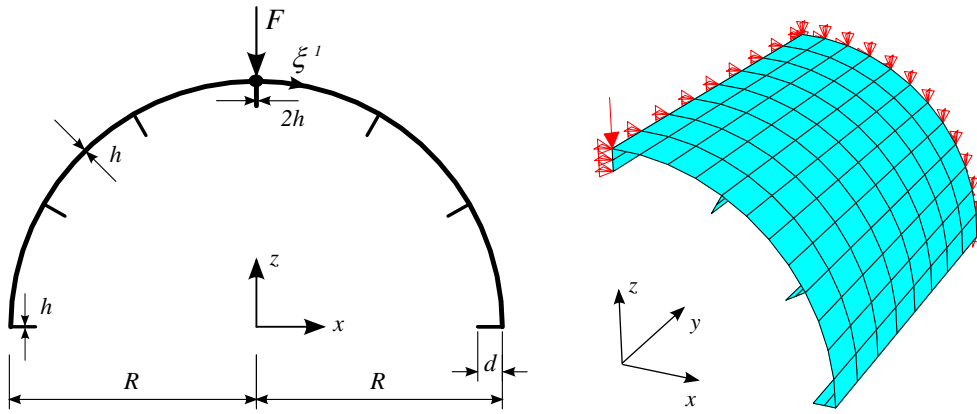


**Fig. 20** Stiffened cylindrical shell and finite element mesh

**Fig. 21**  $u_z$  in mm for the present formulation

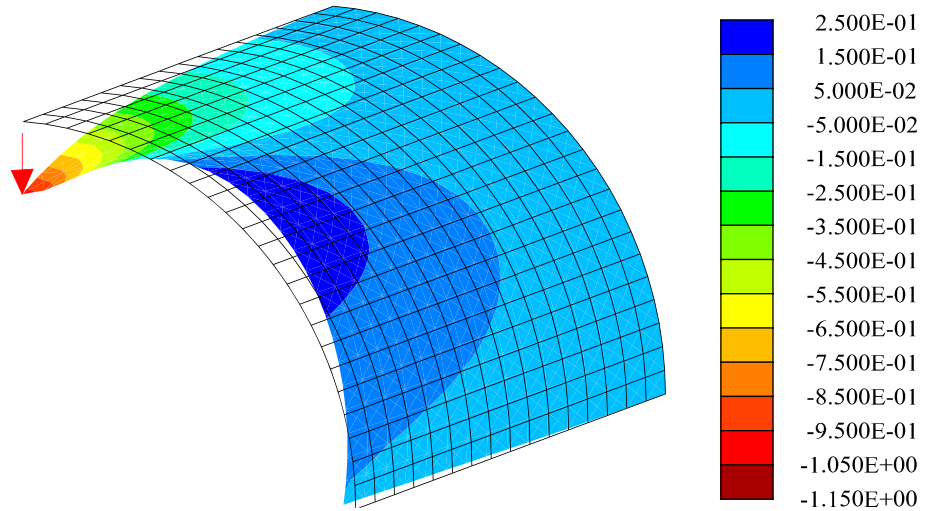
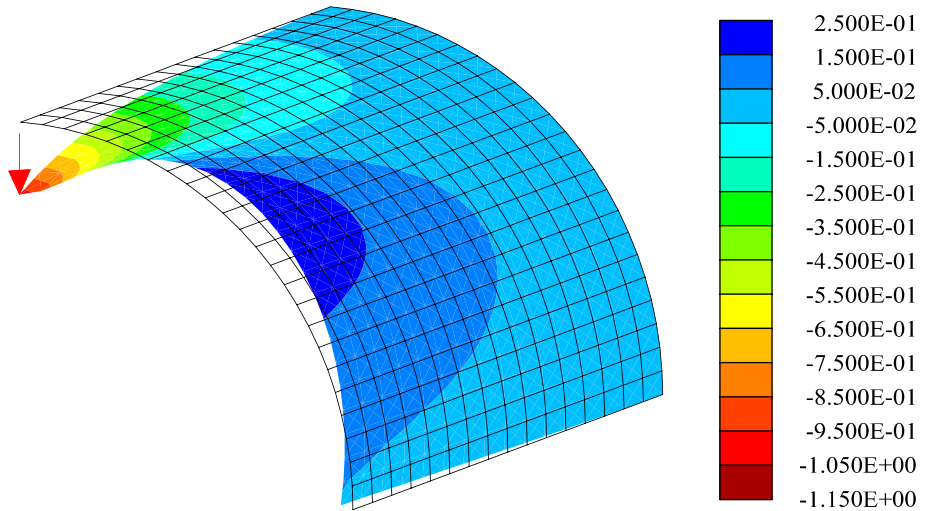


**Fig. 22**  $u_z$  in mm for the element formulation [7]



(64) are taken. Comparative results are obtained with the element formulation [7] where the transverse shear stresses are computed within a post processing procedure and thus are not embedded in the variational formulation. Plots of the dis-

placements  $u_z(\xi^1, \xi^2)$  and of the shear stresses  $\tau_{13}(\xi^1, \xi^2)$  of the middle surface, where  $\xi^2 \equiv y$ , are depicted in Figs. 21, 22, 23, and 24 for the present model and the comparative model. A  $24 \times 16$  mesh is used for the skin and a  $2 \times 16$

**Fig. 23**  $\tau_{13}$  of the middle surface in  $\text{N/mm}^2$  for the present formulation

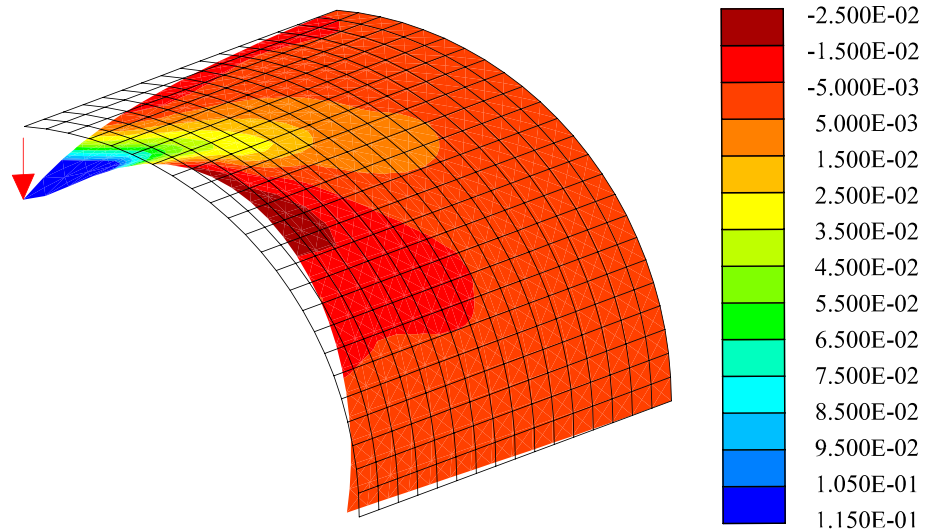


**Fig. 24**  $\tau_{13}$  of the middle surface in  $\text{N/mm}^2$  for the element formulation [7]

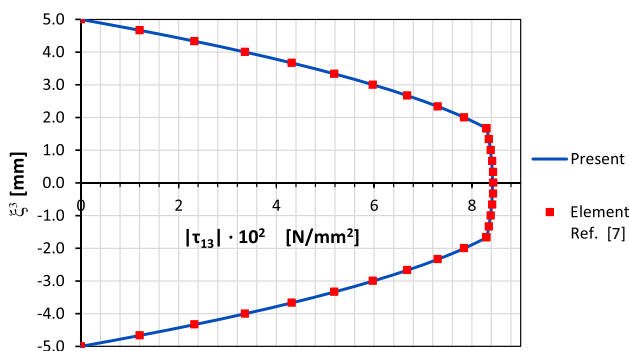
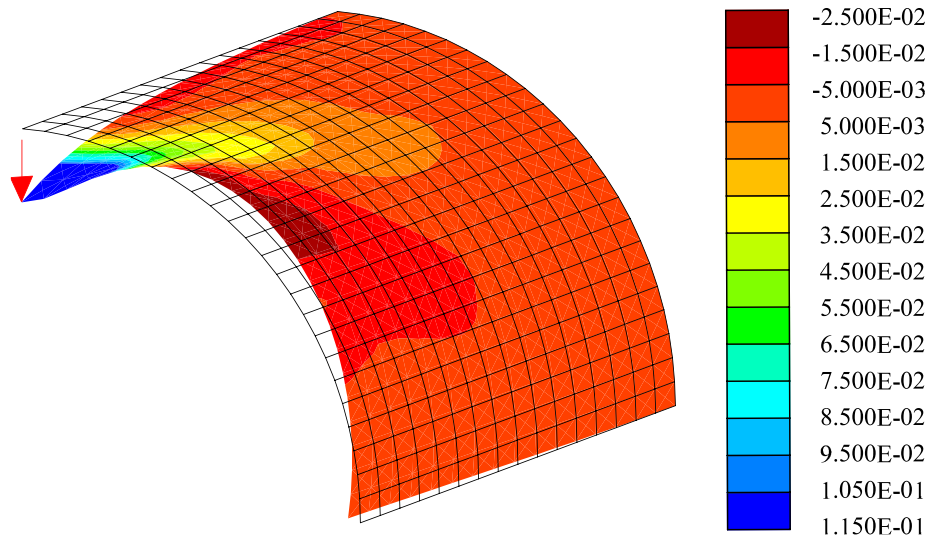


**Fig. 25**  $\tau_{13}(\xi_p^1, \xi_p^2, \xi^3)$  of the stiffened cylindrical shell

mesh vor each stiffener. The displacements of the deformed configuration are amplified by a factor 200 and the stiffeners are turned off in the plots. Finally in Fig. 25 the shape of  $\tau_{13}(\xi_p^1, \xi_p^2)$  through the thickness at a point  $P$  with coordinates  $\xi_p^1 = (27/192 \cdot \pi/2) \cdot R$  and  $\xi_p^2 = 13/128 \cdot L$  is

displayed. Here, a refined mesh with  $96 \times 64$  elements for the skin and  $2 \times 64$  elements for each stiffener is used. In all diagrams one can state good agreement between the two models.

### 5 Conclusions

In this paper a new mixed hybrid 4-node finite element for applications to layered shells is presented. The global shell equations in terms of stress resultants are coupled with the local equilibrium equations in the variational formulation. With layerwise cubic interpolation functions one obtains automatically continuous interlaminar shear stresses. Furthermore the stress boundary conditions at the outer surfaces are automatically fulfilled. This holds also for the integrals of the shear stresses which coincide identically with the independently interpolated shear forces. Good agreement of the displacements and stresses with comparative results is

obtained. The setup of the element stiffness matrix is computationally effective, since the matrix which is subject to a static condensation is sparse. The essential feature of the element formulation is the fact that it leads to the usual shell degrees of freedom. This allows the application of standard boundary conditions and the computation of folded shell structures.

**Acknowledgments** The financial support of the Deutsche Forschungsgemeinschaft (DFG) for the third author is gratefully acknowledged.

## Appendix 1: Data for some selected stress distributions

### Symmetric cross-ply laminate $[0^\circ/90^\circ/0^\circ]$

**Table 3**  $\tau_{xz}$  at  $(x_p = 21.429 \text{ mm}, y_p = 0, z)$  for a cross-ply laminate  $[0^\circ/90^\circ/0^\circ]$ , see Fig. 7

$z$ (mm)	Present (N/mm <sup>2</sup> )	Solid shell [29] (N/mm <sup>2</sup> )
0.000	30.3479	30.3950
0.033	30.3313	30.3772
0.067	30.2814	30.3240
0.100	30.1984	30.2355
0.133	30.0821	30.1118
0.167	29.9326	29.5985
0.167	29.9326	29.5985
0.200	28.2863	28.2535
0.233	26.3407	26.2993
0.267	24.0957	24.0466
0.300	21.5514	21.4958
0.333	18.7078	18.6469
0.367	15.5649	15.5003
0.400	12.1227	12.0566
0.433	8.3811	8.3166
0.467	4.3402	4.2812
0.500	0.0000	–

**Table 4**  $\tau_{yz}$  at  $(x_p = 0, y_p = 21.429 \text{ mm}, z)$  for a cross-ply laminate  $[0^\circ/90^\circ/0^\circ]$ , see Fig. 8

$z$ (mm)	Present (N/mm <sup>2</sup> )	Solid shell [29] (N/mm <sup>2</sup> )
0.000	11.8232	11.8505
0.033	11.5727	11.5922

**Table 4** continued

$z$ (mm)	Present (N/mm <sup>2</sup> )	Solid shell [29] (N/mm <sup>2</sup> )
0.067	10.8213	10.8181
0.100	9.5688	9.5305
0.133	7.8153	7.7330
0.167	5.5609	6.0371
0.167	5.5609	6.0371
0.200	5.2550	5.2004
0.233	4.8936	4.8406
0.267	4.4765	4.4263
0.300	4.0038	3.9573
0.333	3.4755	3.4335
0.367	2.8917	2.8548
0.400	2.2522	2.2211
0.433	1.5570	1.5326
0.467	0.8063	0.7892
0.500	0.0000	–

### Unsymmetric cross-ply laminate $[0^\circ/90^\circ]$

**Table 5**  $\tau_{xz}$  at  $(x_p = 21.429 \text{ mm}, y_p = 0, z)$  for an unsymmetric lay-up  $[0^\circ/90^\circ]$ , see Fig. 11

$z$ (mm)	Present (N/mm <sup>2</sup> )	Solid shell [29] (N/mm <sup>2</sup> )
–0.50	0.0000	0.0000
–0.45	7.9417	8.1903
–0.40	14.4393	15.0640
–0.35	19.4926	20.3502
–0.30	23.1018	24.0410
–0.25	25.2668	26.1316
–0.20	25.9875	26.6204
–0.15	25.2641	25.5085
–0.10	23.0965	22.7998
–0.05	19.4847	18.5014
0.00	14.4287	14.3302
0.00	14.4287	14.3302
0.05	13.7072	12.4583
0.10	12.8254	11.8661
0.15	11.7833	11.0749
0.20	10.5808	10.0846
0.25	9.2181	8.8955
0.30	7.6951	7.5076
0.35	6.0118	5.9208
0.40	4.1682	4.1351
0.45	2.1642	2.1505
0.50	0.0000	–



**Angle-ply laminate with 3 layers [45°/−45°/45°]**

**Table 6**  $\tau_{xz}$  at  $(x_p = 21.429 \text{ mm}, y_p = 0, z)$  for an angle ply lay-up [45°/−45°/45°], see Fig. 13

z (mm)	Present (N/mm <sup>2</sup> )	Solid shell [29] (N/mm <sup>2</sup> )
0.000	23.9516	23.6254
0.033	23.6811	23.3621
0.067	22.8694	22.5779
0.100	21.5166	21.2889
0.133	19.6227	19.5173
0.167	17.1877	17.6660
0.167	17.1877	17.6660
0.200	16.2424	16.3040
0.233	15.1252	15.1801
0.267	13.8361	13.8798
0.300	12.3752	12.4176
0.333	10.7423	10.7934
0.367	8.9376	9.0044
0.400	6.9610	7.0428
0.433	4.8126	4.8945
0.467	2.4922	2.5393
0.500	0.0000	–

**Table 7**  $\tau_{xz}$  at  $(x_p = 10.937 \text{ mm}, y_p = 14.062 \text{ mm}, z)$  for an angle ply lay-up [45°/−45°/45°], see Fig. 14

z (mm)	Present (N/mm <sup>2</sup> )	Solid shell [29] (N/mm <sup>2</sup> )
0.000	9.3008	9.1705
0.033	9.3478	9.2315
0.067	9.4887	9.4141
0.100	9.7237	9.7164
0.133	10.0526	10.1315
0.167	10.4755	10.3575
0.167	10.4755	10.3575
0.200	9.8993	10.0405
0.233	9.2184	9.3620
0.267	8.4328	8.5677
0.300	7.5424	7.6645
0.333	6.5472	6.6531
0.367	5.4473	5.5339
0.400	4.2426	4.3068
0.433	2.9331	2.9715
0.467	1.5189	1.5289
0.500	0.0000	–

**Table 8**  $\tau_{yz}$  at  $(x_p = 10.937 \text{ mm}, y_p = 14.062 \text{ mm}, z)$  for an angle ply lay-up [45°/−45°/45°], see Fig. 15

z (mm)	Present (N/mm <sup>2</sup> )	Solid shell [29] (N/mm <sup>2</sup> )
0.000	13.0392	12.9990
0.033	12.9901	12.9394
0.067	12.8428	12.7611
0.100	12.5973	12.4656
0.133	12.2535	12.0560
0.167	11.8115	11.5437
0.167	11.8115	11.5437
0.200	11.1618	10.9263
0.233	10.3941	10.1851
0.267	9.5082	9.3202
0.300	8.5043	8.3376
0.333	7.3822	7.2376
0.367	6.1420	6.0203
0.400	4.7836	4.6856
0.433	3.3072	3.2335
0.467	1.7127	1.6642
0.500	0.0000	–

**Appendix 2: Interpolation matrices of the mixed element formulation**

The transverse shear strains at the midside nodes  $A, B, C, D$  of the element are as follows

$$\begin{aligned} \gamma_{\xi}^M &= [\mathbf{u}_{,\xi} \cdot \bar{\mathbf{D}} + \mathbf{X}_{,\xi} \cdot \Delta \mathbf{d}]^M & M &= B, D \\ \gamma_{\eta}^L &= [\mathbf{u}_{,\eta} \cdot \bar{\mathbf{D}} + \mathbf{X}_{,\eta} \cdot \Delta \mathbf{d}]^L & L &= A, C \end{aligned} \tag{66}$$

where the following quantities are given with the bilinear interpolation (44)–(47)

$$\begin{aligned} \bar{\mathbf{D}}^A &= \frac{1}{2} (\bar{\mathbf{D}}_4 + \bar{\mathbf{D}}_1) & \Delta \mathbf{d}^A &= \frac{1}{2} (\Delta \mathbf{d}_4 + \Delta \mathbf{d}_1) \\ \bar{\mathbf{D}}^B &= \frac{1}{2} (\bar{\mathbf{D}}_1 + \bar{\mathbf{D}}_2) & \Delta \mathbf{d}^B &= \frac{1}{2} (\Delta \mathbf{d}_1 + \Delta \mathbf{d}_2) \\ \bar{\mathbf{D}}^C &= \frac{1}{2} (\bar{\mathbf{D}}_2 + \bar{\mathbf{D}}_3) & \Delta \mathbf{d}^C &= \frac{1}{2} (\Delta \mathbf{d}_2 + \Delta \mathbf{d}_3) \\ \bar{\mathbf{D}}^D &= \frac{1}{2} (\bar{\mathbf{D}}_3 + \bar{\mathbf{D}}_4) & \Delta \mathbf{d}^D &= \frac{1}{2} (\Delta \mathbf{d}_3 + \Delta \mathbf{d}_4) \\ \mathbf{X}_{,\eta}^A &= \frac{1}{2} (\mathbf{X}_4 - \mathbf{X}_1) & \mathbf{u}^A_{,\eta} &= \frac{1}{2} (\mathbf{u}_4 - \mathbf{u}_1) \\ \mathbf{X}_{,\xi}^B &= \frac{1}{2} (\mathbf{X}_2 - \mathbf{X}_1) & \mathbf{u}^B_{,\xi} &= \frac{1}{2} (\mathbf{u}_2 - \mathbf{u}_1) \\ \mathbf{X}_{,\eta}^C &= \frac{1}{2} (\mathbf{X}_3 - \mathbf{X}_2) & \mathbf{u}^C_{,\eta} &= \frac{1}{2} (\mathbf{u}_3 - \mathbf{u}_2) \\ \mathbf{X}_{,\xi}^D &= \frac{1}{2} (\mathbf{X}_3 - \mathbf{X}_4) & \mathbf{u}^D_{,\xi} &= \frac{1}{2} (\mathbf{u}_3 - \mathbf{u}_4). \end{aligned} \tag{67}$$

The matrix  $\mathbf{B} = [\mathbf{B}_1, \mathbf{B}_2, \mathbf{B}_3, \mathbf{B}_4]$  follows with

$$\mathbf{B}_I = \begin{bmatrix} N_{I,1} \mathbf{X}_{,1}^T & \mathbf{0} \\ N_{I,2} \mathbf{X}_{,2}^T & \mathbf{0} \\ N_{I,1} \mathbf{X}_{,2}^T + N_{I,2} \mathbf{X}_{,1}^T & \mathbf{0} \\ N_{I,1} \bar{\mathbf{D}}_{,1}^T & N_{I,1} \mathbf{b}_{I1}^T \\ N_{I,2} \bar{\mathbf{D}}_{,2}^T & N_{I,2} \mathbf{b}_{I2}^T \\ N_{I,1} \bar{\mathbf{D}}_{,2}^T + N_{I,2} \bar{\mathbf{D}}_{,1}^T & N_{I,1} \mathbf{b}_{I2}^T + N_{I,2} \mathbf{b}_{I1}^T \\ \mathbf{J}^{-1} \begin{Bmatrix} N_{I,\xi} \bar{\mathbf{D}}_{,M}^T \\ N_{I,\eta} \bar{\mathbf{D}}_{,L}^T \end{Bmatrix} & \mathbf{J}^{-1} \begin{Bmatrix} N_{I,\xi} \xi_I \mathbf{b}_{,M}^T \\ N_{I,\eta} \eta_I \mathbf{b}_{,L}^T \end{Bmatrix} \end{bmatrix} \quad (68)$$

We denote by  $\mathbf{b}_{I\alpha} = \mathbf{T}_I^T \mathbf{X}_{,\alpha}$ ,  $\mathbf{b}_M = \mathbf{T}_I^T \mathbf{X}^M_{,\xi}$  and  $\mathbf{b}_L = \mathbf{T}_I^T \mathbf{X}^L_{,\eta}$ , where  $\mathbf{T}_I$  is introduced in (50). The allocation of the midside nodes to the corner nodes is given by  $(I, M, L) \in \{(1, B, A); (2, B, C); (3, D, C); (4, D, A)\}$ . To alleviate the notation the superscript  $h$  is omitted in the matrix.

According to [32] the interpolation matrix  $\mathbf{N}_\sigma$  reads

$$\mathbf{N}_\sigma = \begin{bmatrix} \mathbf{1}_3 & \mathbf{0} & \mathbf{0} & \mathbf{N}_\sigma^m & \mathbf{0} & \mathbf{0} \\ \mathbf{0} & \mathbf{1}_3 & \mathbf{0} & \mathbf{0} & \mathbf{N}_\sigma^b & \mathbf{0} \\ \mathbf{0} & \mathbf{0} & \mathbf{1}_2 & \mathbf{0} & \mathbf{0} & \mathbf{N}_\sigma^s \end{bmatrix} \quad (69)$$

where

$$\mathbf{N}_\sigma^m = \mathbf{N}_\sigma^b = \mathbf{T}_\sigma^0 \begin{bmatrix} \eta - \bar{\eta} & 0 \\ 0 & \xi - \bar{\xi} \\ 0 & 0 \end{bmatrix}$$

$$\mathbf{N}_\sigma^s = \tilde{\mathbf{T}}_\sigma^0 \begin{bmatrix} \eta - \bar{\eta} & 0 \\ 0 & \xi - \bar{\xi} \end{bmatrix} \quad (70)$$

with the coordinates  $\bar{\xi} = \frac{1}{A_e} \int_{\Omega_e} \xi \, dA$  and  $\bar{\eta} = \frac{1}{A_e} \int_{\Omega_e} \eta \, dA$

as well as

$$\mathbf{T}_\sigma^0 = \begin{bmatrix} J_{11}^0 J_{11}^0 & J_{21}^0 J_{21}^0 & 2J_{11}^0 J_{21}^0 \\ J_{12}^0 J_{12}^0 & J_{22}^0 J_{22}^0 & 2J_{12}^0 J_{22}^0 \\ J_{11}^0 J_{12}^0 & J_{21}^0 J_{22}^0 & J_{11}^0 J_{22}^0 + J_{12}^0 J_{21}^0 \end{bmatrix}$$

$$\tilde{\mathbf{T}}_\sigma^0 = \begin{bmatrix} J_{11}^0 & J_{21}^0 \\ J_{12}^0 & J_{22}^0 \end{bmatrix} \quad (71)$$

The constants  $J_{\alpha\beta}^0 = J_{\alpha\beta}(\xi = 0, \eta = 0)$  are the components of  $\mathbf{J}$  in Eq. (46) evaluated at the element centre.

Again from [32] it holds for  $\mathbf{N}_\varepsilon^1$

$$\mathbf{N}_\varepsilon^1 = \begin{bmatrix} \mathbf{1}_3 & \mathbf{0} & \mathbf{0} & \mathbf{N}_\varepsilon^{m1} & \mathbf{0} & \mathbf{0} \\ \mathbf{0} & \mathbf{1}_3 & \mathbf{0} & \mathbf{0} & \mathbf{N}_\varepsilon^{b1} & \mathbf{0} \\ \mathbf{0} & \mathbf{0} & \mathbf{1}_2 & \mathbf{0} & \mathbf{0} & \mathbf{N}_\varepsilon^{s1} \end{bmatrix} \quad (72)$$

where

$$\mathbf{N}_\varepsilon^{m1} = \mathbf{N}_\varepsilon^{b1} = \mathbf{T}_\varepsilon^0 \begin{bmatrix} \eta - \bar{\eta} & 0 \\ 0 & \xi - \bar{\xi} \\ 0 & 0 \end{bmatrix} \quad \mathbf{N}_\varepsilon^{s1} = \mathbf{N}_\varepsilon^s \quad (73)$$

and

$$\mathbf{T}_\varepsilon^0 = \begin{bmatrix} J_{11}^0 J_{11}^0 & J_{21}^0 J_{21}^0 & J_{11}^0 J_{21}^0 \\ J_{12}^0 J_{12}^0 & J_{22}^0 J_{22}^0 & J_{12}^0 J_{22}^0 \\ 2J_{11}^0 J_{12}^0 & 2J_{21}^0 J_{22}^0 & J_{11}^0 J_{22}^0 + J_{12}^0 J_{21}^0 \end{bmatrix} \quad (74)$$

A further part with special interpolation functions has been introduced in [32] to improve the membrane and bending behaviour of the element. These functions are constructed orthogonal to the stress resultant interpolation. For the sake of convenience this part is omitted here.

### References

- Carrera E (2003) Theories and finite elements for multilayered plates and shells: a unified compact formulation with numerical assessment and benchmarking. Arch Comput Methods Eng 10(3):215–296
- Mittelstedt C, Becker W (2004) Interlaminar stress concentrations in layered structures, Part I: A selective literature survey on the free-edge effect since 1967. J Compos Mater 38:1037–1062
- Zhang Y, Yang C (2009) Recent developments in finite element analysis for laminated composite plates. Compos Struct 88:147–157
- Carrera E, Cinefra M, Petrolo M, Zappino E (2014) Finite element analysis of structures through unified formulation. Wiley, Chichester
- Carrera E, Cinefra M, Lamberti A, Petrolo M (2015) Results on best theories for metallic and laminated shells including layer-wise models. Compos Struct 126:285–298
- Rolfes R, Rohwer K (1997) Improved transverse shear stresses in composite finite elements based on first order shear deformation theory. Int J Numer Methods Eng 40:51–60
- Schürg M, Wagner W, Gruttmann F (2009) An enhanced FSDT model for the calculation of interlaminar shear stresses in composite plate structures. Comput Mech 44(6):765–776
- Noor AK, Burton WS, Peters JM (1990) Predictor–corrector procedure for stress and free vibration analyses of multilayered composite plates and shells. Comput Methods Appl Mech Eng 82:341–364
- Noor AK, Kim YH, Peters JM (1994) Transverse shear stresses and their sensitivity coefficients in multilayered composite panels. AIAA J 2:1259–1269
- Manjunatha BS, Kant T (1994) On evaluation of transverse stresses in layered symmetric composite and sandwich laminates under flexure. Eng Comput 10:499–518
- Vidal P, Gallimard L, Polit O (2013) Proper generalized decomposition and layer-wise approach for the modeling of composite plate structures. Int J Solids Struct 50:2239–2250
- Auricchio F, Sacco E (1999) A mixed-enhanced finite-element for the analysis of laminated composite plates. Int J Numer Methods Eng 44:1481–1504
- Auricchio F, Sacco E, Vairo G (2006) A mixed FSDT finite element for monoclinic laminated plates. Comput Struct 84:624–639
- Auricchio F, Balduzzi G, Khoshgoftar MJ, Rahimi G, Sacco E (2014) Enhanced modeling approach for multilayer anisotropic plates based on dimension reduction method and Hellinger–Reissner principle. Compos Struct 118:622–633
- Carrera E (1996)  $C^0$  Reissner–Mindlin multilayered plate elements including zig-zag and interlaminar stress continuity. Int J Numer Methods Eng 39:1797–1820

16. Brank B, Carrera E (2000) Multilayered shell finite element with interlaminar continuous shear stresses: a refinement of the Reissner–Mindlin formulation. *Int J Numer Methods Eng* 48:843–874
17. Carrera E (2003) Historical review of zig-zag theories for multilayered plates and shells. *Appl Mech Rev* 56:237–308
18. Reddy JN (1984) A simple high-order theory for laminated composite plates. *J Appl Mech* 51:745–752
19. Ferreira A (2005) Analysis of composite plates using a layerwise shear deformation theory and multiquadratics discretization. *Mech Adv Mater Struct* 12:99–112
20. Moleiro F, Mota Soares CM, Mota Soares CA, Reddy JN (2011) A layerwise mixed least-squares finite element model for static analysis of multilayered composite plates. *Comput Struct* 89:1730–1742
21. Engblom JJ, Ochoa OO (1985) Through-the-thickness stress distribution for laminated plates of advanced composite materials. *Int J Numer Methods Eng* 21:1759–1776
22. Reddy JN (1989) On refined computational models of composite laminates. *Int J Numer Methods Eng* 27:361–382
23. Rao KM, Meyer-Piening HR (1990) Analysis of thick laminated anisotropic composite plates by the finite element method. *Compos Struct* 15:185–213
24. Robbins DH, Reddy JN (1993) Modelling of thick composites using a layerwise laminate theory. *Int J Numer Methods Eng* 36:655–677
25. Topdar P, Sheikh AH, Dhang N (2003) Finite element analysis of composite and sandwich plates using a continuous interlaminar shear stress model. *J Sandw Struct Mat* 5:207–231
26. Gruttmann F, Wagner W (1994) On the numerical analysis of local effects in composite structures. *Compos Struct* 29:1–12
27. Gruttmann F, Wagner W (1996) Coupling of 2d- and 3d-composite shell elements in linear and nonlinear applications. *Comput Methods Appl Mech Eng* 129:271–287
28. Marimuthu R, Sundaresan MK, Rao GV (2003) Estimation of interlaminar stresses in laminated plates subjected to transverse loading using three-dimensional mixed finite element formulation. *The Institution of Engineers (India). Tech J Aerosp Eng* 84:1–8
29. Klinkel S, Gruttmann F, Wagner W (1999) A continuum based 3D-shell element for laminated structures. *Comput Struct* 71:43–62
30. Klinkel S, Gruttmann F, Wagner W (2006) A robust non-linear solid shell element based on a mixed variational formulation. *Comput Methods Appl Mech Eng* 195:179–201
31. Wagner W, Gruttmann F (2005) A robust nonlinear mixed hybrid quadrilateral shell element. *Int J Numer Methods Eng* 64:635–666
32. Gruttmann F, Wagner W (2006) Structural analysis of composite laminates using a mixed hybrid shell element. *Comput Mech* 37:479–497
33. Dvorkin E, Bathe KJ (1984) A continuum mechanics based four node shell element for general nonlinear analysis. *Eng Comput* 1:77–88
34. Taylor RL (2015) FEAP. <http://www.ce.berkeley.edu/projects/feap/>
35. MacNeal RH, Harder RL (1985) A proposed standard set of problems to test finite element accuracy. *Finite Elem Anal Des* 1:3–20